

# Gravitationally lensed quasars in *Gaia* - IV. 150 new lenses, quasar pairs, and projected quasars

C. Lemon<sup>1</sup>★, T. Anguita<sup>2,3</sup>, M. Auger<sup>4,5</sup>, F. Courbin<sup>1</sup>, A. Galan<sup>1</sup>, R. McMahon<sup>4,5</sup>,  
F. Neira<sup>2,3</sup>, M. Oguri<sup>6,7</sup>, P. Schechter<sup>8,9</sup>, A. Shajib<sup>10,11</sup>†, and T. Treu<sup>11</sup>

<sup>1</sup>*Institute of Physics, Laboratoire d'Astrophysique, Ecole Polytechnique Fédérale de Lausanne (EPFL), Observatoire de Sauverny, CH-1290 Versoix, Switzerland*

<sup>2</sup>*Departamento de Ciencias Físicas, Universidad Andres Bello, Fernandez Concha 700, Las Condes, Santiago, Chile*

<sup>3</sup>*Millennium Institute of Astrophysics, Monseñor Nuncio Sotero Sanz 100, Oficina 104, 7500011 Providencia, Santiago, Chile*

<sup>4</sup>*Institute of Astronomy, University of Cambridge, Madingley Road, Cambridge CB3 0HA, UK*

<sup>5</sup>*Kavli Institute for Cosmology, University of Cambridge, Madingley Road, Cambridge CB3 0HA, UK*

<sup>6</sup>*Center for Frontier Science, Chiba University, 1-33 Yayoi-cho, Inage-ku, Chiba 263-8522, Japan*

<sup>7</sup>*Department of Physics, Graduate School of Science, Chiba University, 1-33 Yayoi-Cho, Inage-Ku, Chiba 263-8522, Japan*

<sup>8</sup>*MIT Kavli Institute for Astrophysics and Space Research, Cambridge, MA 02139 USA*

<sup>9</sup>*MIT Department of Physics, Cambridge, MA 02139 USA*

<sup>10</sup>*Department of Astronomy and Astrophysics, University of Chicago, Chicago, IL 60637, USA*

<sup>11</sup>*Department of Physics and Astronomy, University of California, Los Angeles, CA 90095, USA*

Accepted XXX. Received YYY; in original form ZZZ

## ABSTRACT

We report the spectroscopic follow-up of 175 lensed quasar candidates selected using *Gaia* Data Release 2 observations following Lemon et al. (2019). Systems include 86 confirmed lensed quasars and a further 17 likely lensed quasars based on imaging and/or similar spectra. We also confirm 11 projected quasar pairs and 11 physical quasar pairs, while 25 systems are left as unclassified quasar pairs – pairs of quasars at the same redshift, which could be either distinct quasars or potential lensed quasars. Especially interesting objects include 8 quadruply imaged quasars of which two have BAL sources, an apparent triple, and a doubly lensed LoBaL quasar. The source redshifts and image separations of these new lenses range between 0.65–3.59 and 0.78–6.23'' respectively. We compare the known population of lensed quasars to an updated mock catalogue at image separations between 1 and 4 arcseconds, showing a very good match at  $z < 1.5$ . At  $z > 1.5$ , only 47% of the predicted number are known, with 56% of these missing lenses at image separations below 1.5''. The missing higher-redshift, small-separation systems will have fainter lensing galaxies, and are partially explained by the unclassified quasar pairs and likely lenses presented in this work, which require deeper imaging. Of the 11 new reported projected quasar pairs, 5 have impact parameters below 10 kpc, almost tripling the number of such systems, which can probe the innermost regions of quasar host galaxies through absorption studies. We also report four new lensed galaxies discovered through our searches, with source redshifts ranging from 0.62 to 2.79.

**Key words:** gravitational lensing: strong – quasars: general – methods: observational

## 1 INTRODUCTION

Gravitationally lensed quasars offer several unique probes of astrophysics and cosmology. Their variable sources allow measurements of the time delays between images, which can be used to constrain the Hubble constant through time-delay cosmography (Shajib et al. 2020; Harvey 2020). The compact nature of the source allows a probe of the mass at compact scales in the lensing galaxy through

microlensing; the brightness variations caused by stars as they pass in front of each quasar image can be used to constrain the Initial Mass Function (Jiménez-Vicente & Mediavilla 2019; Schechter et al. 2014) and place limits on the abundance of primordial black holes (Mediavilla et al. 2017). Simultaneously, microlensing can constrain the innermost structure of quasars at high-redshift (Hutsemékers & Sluse 2021; Paic et al. 2022). The particular brightness of quasar sources provides an excellent tool for studying the geometry and kinematics of intervening matter (Rubin et al. 2018; Okoshi et al. 2021; Lemon et al. 2022). This brightness also means that lensed quasars are often source-selected (Myers et al. 2003; Oguri

★ E-mail: cameron.lemon@epfl.ch

† NHFP Einstein Fellow

et al. 2006), in contrast with lensed galaxy samples which are selected through their bright lensing galaxies. This offers a chance to create a well-defined statistical sample down to small separations, which can be used to probe cosmology and galaxy evolution parameters (Chae 2003; Oguri et al. 2012). These studies are often limited by the small number of lenses that suit their particular purpose, for example requiring four well-separated images with time delays above 10 days for time-delay cosmography.

Recent optical to near-infrared surveys now provide an efficient way to select high-confidence quasar candidates across the whole sky (e.g. Stern et al. 2012), and have the resolution and depth to identify whether such systems are lensed, i.e. whether there are multiple images and a lensing galaxy present (e.g. Chan et al. 2022). However, lensed quasars are particularly rare, and outnumbered by convincing contaminant systems, mainly composed of compact star-forming galaxies and chance quasar/star projections (Treu et al. 2018). The all-sky space-based catalogues from *Gaia* offer a particularly effective way of removing these contaminants. In the previous papers of this series, we have shown that combining the *Gaia* catalogue detections and parameters with WISE and ground-based optical imaging can efficiently remove the common contaminants of lensed quasar searches (Lemon et al. 2017, 2018, 2019). In this paper, we continue our spectroscopic follow-up campaign of lensed quasar candidates selected with the techniques developed in these papers.

In Section 2, we describe the selection techniques and datasets used for candidate selection. Follow-up spectroscopy and imaging are described in Section 3. Section 4 details the characteristics of individual systems, and a general discussion on the samples and sub-samples are discussed in Section 5. We conclude in Section 6.

## 2 CANDIDATE SELECTION

Candidates were selected following Lemon et al. (2019), and represent the follow-up of different Right Ascension and Declination ranges, as well as untargeted systems in previously covered sky, due to lack of spectroscopic follow-up time. Two searches begin from a catalogue of quasars and quasar candidates. For these searches we used the Milliquas catalogue (Flesch 2015), which consists of confirmed quasars and highly likely quasar candidates based on X-ray, radio, and optical and infrared colour selection. We supplement this catalogue with objects using colours from the Wide-field Infrared Survey Explorer (WISE). We take objects with  $W1-W2 > 0.4$  (in Vega), which is less strict than most quasar selections in order to include systems with possibly large contamination from the lensing galaxy, or sources with non-standard quasar colours. Our final search begins from a morphological galaxy catalogue. Below, we briefly describe the selection techniques for lensed quasars within these quasar and galaxy samples, making use of *Gaia* data release 2 (GDR2, Gaia Collaboration et al. 2018). Further details on selection numbers and completeness of recovering existing samples can be found in Lemon et al. (2019).

### 2.1 Multiple *Gaia* detections around quasar catalogues

This search is refined from that originally performed in Lemon et al. (2018), namely searching for multiple *Gaia* detections around red ALLWISE detections (Mainzer et al. 2011). The search consists of visually inspecting ground-based colour images of systems satisfying varying  $W1-W2$  colour cuts, local stellar densities and thresholds on the significance of proper motion for the different

numbers of *Gaia* detections associated to the system. The Milliquas catalogue is also used as a starting catalogue for this selection.

### 2.2 Modelling unWISE pixels

The main contaminants of the search detailed above are quasar+star projections, since they will have multiple *Gaia* detections, often lacking the necessary proper motion precision to remove the star as a moving object, and having quasar-like colours in the infrared, radio, or X-ray due to blending issues in WISE (PSF FWHM of  $\sim 5''$ ). Ground-based imaging can often rule out such pairs through optical colour differences or a lack of a lensing galaxy, however contaminants still remain and the number of objects is too large to visually inspect. Lemon et al. (2019) introduced a forced model fitting of WISE data based on *Gaia* positions to extract the infrared colours of nearby point sources and thus classify the multiple components within such systems. We used the unWISE W1 and W2 data (Lang et al. 2016), an unblurred coaddition of all WISE data to-date. Following local *Gaia* density cuts, proper motion significance cuts, and finally cuts in the  $G-W1$  vs.  $W1-W2$  colour space, we obtained a classification procedure to retain nearly 99 per cent of known lensed quasars, while removing  $\sim 80$  per cent of previously followed-up contaminants.

### 2.3 *Gaia* detections offset from LRGs

Since both search techniques presented above rely heavily on source selection, we also investigate using galaxies as a starting catalogue. We use spectroscopic galaxies from SDSS DR12, and keep all systems with one *Gaia* detection within 1 and  $3.5''$ , or two *Gaia* detections within  $4.5''$  (and separated by less than  $4.5''$ ). The need for the single detection to be further than  $1''$  is based on known lensed quasars satisfying such a constraint, and reduces contamination. We also use morphological galaxies from Pan-STARRS, requiring at least one *Gaia* detection between 1 and  $3''$  away. Proper motion and astrometric excess noise cuts are performed on all matching *Gaia* detections to further remove contamination from stars and star-forming galaxies.

## 3 OBSERVATIONS

### 3.1 Spectroscopy

#### 3.1.1 William Herschel Telescope: ISIS

55 systems were observed with the Intermediate-dispersion Spectrograph and Imaging System (ISIS) on the WHT on the nights of 11-12 Feb. 2019. The R158R and R300B gratings were used for the red and blue arms respectively, with the standard  $5300\text{\AA}$  dichroic and GG495 second order cut filter in the red arm. This provided dispersions of  $1.81\text{\AA pixel}^{-1}$  and  $0.86\text{\AA pixel}^{-1}$  for the red and blue arms.

#### 3.1.2 Nordic Optical Telescope: ALFOSC

43 systems were observed with grism #4 and the Alhambra Faint Object Spectrograph and Camera (ALFOSC) on the NOT on 1-2 October 2019, providing a dispersion of  $3.3\text{\AA pixel}^{-1}$ . All spectra were reliably deblended, except J2017+6204, for which high-resolution imaging confirms it as a lensed quasar.

### 3.1.3 New Technology Telescope: EFOSC2

79 systems were observed with grism #13 of the ESO Faint Object Spectrograph and Camera version 2 (EFOSC2) over four runs (NTT1, 0104.A-0194(A): 22-24 Oct. 2019; NTT2, 0104.A-0194(B): 18-20 Jan. 2020; NTT3, 106.218K.001: 19-21 Oct. 2020; and NTT4, 106.218K.002: 15-17 Jan. 2021), providing a dispersion of  $2.77\text{\AA pixel}^{-1}$ .

### 3.1.4 General reduction procedure

Since several spectrographs were used for long-slit spectroscopic follow-up of our candidates, we give a brief description of the common steps. The extraction follows that outlined in Lemon et al. (2022), and fits multiple Moffat components, the parameters for which are determined from the binned data themselves. In particular, the following steps are taken:

- After bias-subtracting each image, cosmic rays are found and masked as all pixels above a certain threshold in the absolute Laplacian of the data. For the brightest objects this value is increased depending upon visual inspection of the cosmic ray mask.
- The sky background is subtracted by determining the median value within the pixels either side of the trace of the object (between 20 and 80 pixels away). We later use this same background to correct the wavelength calibration to bright sky lines. The region is also used to determine the sky background noise at each spectral pixel (i.e., wavelength).
- A Poisson noise map is created using the detector gain, and added in quadrature with the sky noise to provide a pixel noise map.
- A wavelength solution is determined from fitting the lines of an arc exposure (HeNe or CuAr) taken the afternoon before observations. An absolute shift is calculated for each exposure by measuring the positions of the Na 5892Å, [O I]-5577Å and 6300Å sky lines. This is often a significant shift ( $\gtrsim 1$  pixel) and shows variation with wavelength, and so absolute wavelength measurements should not be trusted to more than the approximate pixel dispersion value of each instrument/grism combination.

## 3.2 Imaging

Deep imaging is key to identifying the lensing galaxy or counter-image in lensed quasar candidates, and thus we use several imaging datasets throughout this work. Principally we use *grizY* imaging from Pan-STARRS (Chambers et al. 2016), and the *grz* imaging from the DESI Legacy Imaging Surveys (Dey et al. 2019). When higher-resolution imaging is required or a system is investigated for other catalogue detections, we check the Canadian Astronomy Data Centre archive, Vizier catalogues within 5 arcseconds (Ochsenbein et al. 2000), and nearby NED detections and associated references. For some quadruply-imaged systems *HST* multi-band imaging and models are presented in Schmidt et al. (2022).

### 3.2.1 General imaging analysis

When analysing individual systems, we often want to fit the pixels with a combination of analytic profiles. Most commonly, we want to identify if a lensing galaxy is present between two bright quasar PSFs. For each image available, we use a nearby star in the field and fit this as a Moffat profile to determine the PSF of the system (Moffat 1969). We then fit a square  $10\times 10''$  cutout around the system, using the relevant number of point sources. This process is performed

simultaneously in all bands (or possibly a single band), and if a galaxy profile is required we use a Sérsic profile (Sérsic 1963). The free parameters are the position(s) of the point sources, the position(s) of the galaxies, and their associated effective radii, Sérsic indices, and ellipticity parameters. To find the best-fit parameters we use the Markov chain Monte Carlo (MCMC) sampler `emcee` Python package (Foreman-Mackey et al. 2013).

## 3.3 Results

The resulting classifications from analysing both the available imaging and spectroscopy of each system are listed in Table 1, with the selection method, maximum image separation, and *Gaia* magnitudes and proper motion significances.

We broadly classify the systems into the following categories: *definite lensed quasars*, *likely lensed quasars* (based on the subjective opinion and experience of the authors), *unclassified quasar pairs* (systems in which two quasars are spectroscopically resolved and are at the same redshift however no convincing lensing galaxy is seen but also for which there is no clear evidence for them being physically distinct quasars), *binary quasars* (Section 5.2), *projected quasars* (Section 5.3), and *contaminant systems* (definitely not lenses). We note that our use of unclassified quasar pairs is akin to Nearly Identical Quasars (NIQs) which has been used in recent literature (e.g. Anguita et al. 2018), however the change is simply to include those systems which have low signal-to-noise data and could readily be classified as a likely lensed quasar or binary quasar given deeper spectra.

Extracted imaging and spectra of systems are respectively shown in Figures 1 and 3 for confirmed lensed, 4 and 5 for likely lensed quasars, and 6 and 7 for unclassified quasar pairs. We also show the spectra for binary quasars and projected quasars in Figures 8 and 9 respectively.

## 4 NOTES ON INDIVIDUAL SYSTEMS

In this section we comment on any interesting aspects of the individual systems, including their photometry, spectra, and mass modelling. We divide the systems into sections based on their final classification.

### 4.1 Confirmed Lensed Quasars

#### 4.1.1 J0030-3358

A jump in the continuum of the fainter image of this double is likely associated to the 4000Å break of the lensing galaxy, as associated Ca H, K and G-band absorption features are also seen, placing the lens at  $z=0.715$ . This is supported by the Legacy Survey photometric redshift estimate of  $0.84\pm 0.06$  (Zhou et al. 2021), with a small discrepancy likely due to blending with the quasar light. There is absorption on the blue side of the Crv line seen in both images, however this could also be attributed to Milky Way absorption since it is coincident with  $z=0$  Ca H and K absorption.

#### 4.1.2 J0116+4052

The spectra show two quasars at  $z=1.85$  with very similar continuum and broad emission line profiles, suggesting the system is a likely lens. Only shallow Pan-STARRS imaging exists for this system and shows no significant residuals upon subtraction of two PSFs.

**Table 1.** Summary of observed targets and results based on spectroscopy and imaging. Selections are abbreviated as follows: W=WISE catalogue, M=Milliquas catalogue with multiple *Gaia* detections (D, T, Q for double, triple, and quartet); GP=*Gaia* singlet offset from a galaxy. Separations are the largest of the *Gaia* separations if more than two *Gaia* DR2 detections are associated to the system, or based on pixel modelling. PMSIG and runs are described in the text.

Name	R.A.	Dec.	Selection	<i>Gaia</i> G	Sep. (")	PMSIG	Run	Classification
J0021+1927	5.4936	19.4646	WD, MD	20.77, 19.96	2.89	1.05, 2.74	NOT	projected QSOs, $z=1.045, 1.09$
J0027+0438	6.9580	4.6443	WD, MD	17.65, 20.18	1.92	0.56, —	NOT	projected QSOs, $z=0.1935, 1.972$
J0029-0414	7.3861	-4.2472	WD, MD	19.27, 20.43	1.11	1.13, —	NTT3	$z=0.518$ QSO + star
J0030-3358	7.6740	-33.9767	GP	20.89	2.03	—	NTT1	lens, $z=1.58, z_{\text{lens}}=0.715$
J0032-4523	8.1130	-45.3884	WD, MD	20.57, 20.21	2.33	0.12, 0.56	NTT3	projected QSOs, $z=1.667, 1.74$
J0041-5350	10.4496	-53.8460	WD, MD	20.79, 20.85	1.06	1.29, —	NTT1	QSO pair, $z=0.55$
J0045-3937	11.3665	-39.6262	WD	19.70, 18.98	1.14	1.39, 0.60	NTT2	lens, $z=1.85$
J0116+4052	19.1635	40.8811	WD, MD	19.84, 18.96	1.28	—, 1.07	NOT	lens, $z=1.85$
J0124-6334	21.0089	-63.5788	WD, MD	20.50, 19.60	0.87	2.63, 5.19	NTT2	NIQ, $z=1.30$
J0125-1012	21.3174	-10.2082	WD, MD	19.26, 20.63	1.12	1.86, —	NTT2	NIQ, $z=1.22$
J0127-1441	21.7854	-14.6886	WD, MD	20.14, 20.53	3.01	0.14, 1.32	NTT3	NIQ, $z=1.754$
J0130+0725	22.5859	7.4212	WD, MD	18.98, 19.65	2.06	1.33, —	NOT	NIQ, $z=1.54$
J0133+0816	23.2695	8.2788	WD, MD	20.24, 20.57	1.55	—, —	NOT	NIQ, $z=1.27$
J0138+4841	24.5914	48.6963	WD	17.45, 16.42	0.69	—, 1.00	NOT	NIQ, $z=1.172$
J0146-6510	26.6467	-65.1799	WD	17.48, 18.71	1.00	3.49, 0.76	NTT1	NIQ, $z=1.255$
J0149-6532	27.2906	-65.5404	GP	20.58	2.74	—	NTT1	lens(?), $z=0.944?, z=0.395$
J0152-2448	28.0797	-24.8105	WD, MD	20.12, 18.66	1.91	3.81, 2.05	NOT	lens, $z=1.69$
J0156-2751	29.1039	-27.8562	WD, MD	20.40, 20.46	1.50	0.68, 1.81	NTT1	lens, $z=2.97$
J0200-1509	30.0872	-15.1609	WD, MD	20.43, 19.72	0.78	—, —	NTT1	lens, $z=1.185$
J0209-3841	32.3047	-38.6961	WD, MD	20.60, 20.21	1.23	1.06, 1.35	NTT1	lens, $z=2.87$
J0221+0555	35.4474	5.9192	WD, MD	19.96, 19.39	0.86	1.08, 1.19	NOT	NIQ, $z=1.52$
J0232-2429	38.0655	-24.4942	WD, MD	18.00, 19.44	1.44	2.01, 2.97	NTT1	lens, $z=1.578$
J0246-0131	41.6793	-1.5305	WD, MD	19.05, 20.10	1.09	4.06, —	NTT2	$z=0.503$ QSO + star
J0247+7706	41.8664	77.1014	WD	19.49, 20.20	1.94	1.30, 1.10	NOT	lens, $z=2.73$
J0247-2646	41.8764	-26.7729	WD	20.49, 20.78	1.22	—, —	NTT1	lens, $z=1.47$
J0247-0800	41.9561	-8.0150	GP	20.55, 20.70	1.68	—, —	NTT2	lens, $z=3.28, z_{\text{lens}}=0.198$
J0247-6349	41.9780	-63.8232	WD, MD	19.78, 20.94	1.49	0.29, —	NTT1	lens, $z=2.295$
J0249+2606	42.4595	26.1141	WD, MD	18.81, 20.15	3.21	2.18, 1.99	NOT	projected QSOs, $z=1.514, 2.68$
J0310-5545	47.7029	-55.7534	GP		3.57		NTT3	lens, $z=2.31, z_{\text{lens}}=0.298$
J0311+0550	47.7708	5.8367	WD, MD	18.36, 20.01	1.36	0.49, 1.21	NOT	NIQ, $z=0.777$
J0315-3522	48.9099	-35.3827	WD, MD	20.22, 17.92	1.30	1.06, 2.18	NTT2	QSO pair, $z=0.457$
J0325-2232	51.4511	-22.5409	WD, MD	19.74, 19.52	1.01	0.28, 1.29	NTT1	lens, $z=1.35$
J0326-3122	51.5284	-31.3816	WD, MD	20.68, 19.47	1.43	2.05, 2.16	NTT3	NIQ, $z=1.345$
J0326-4950	51.7287	-49.8337	WD, MD	19.68, 20.36	1.63	1.25, 0.64	NTT2	$z=0.229$ GAL + $z=1.72$ QSO
J0329-0208	52.4280	-2.1379	WD	19.99, 19.80	1.32	0.69, 0.25	NTT3	lens, $z=1.352$
J0332-6608	53.0841	-66.1400	WD, MD	18.30, 19.46	0.94	7.98, 1.90	NTT2	NIQ, $z=1.97$
J0336-3244	54.0816	-32.7410	WD	20.78, 18.13	1.29	—, 5.21	NTT2	$z=0.565$ QSO + other
J0339-6121	54.7870	-61.3625	WD	18.62, 19.52	1.26	0.30, 0.83	NTT1	lens, $z=2.89$
J0346+2154	56.5458	21.9124	WD, MD	18.98, 18.76	0.99	—, 4.55	NOT	NIQ, $z=2.365$
J0346-6414	56.5579	-64.2417	GP	19.41	1.91	—	NTT1	lens, $z=2.96$
J0347-2154	56.7690	-21.9095	GP	20.01, 19.46	1.87	—, 2.38	WHT/NTT1	lens, $z=0.81, z_{\text{lens}}=0.187$
J0350-4611	57.7146	-46.1858	WD, MD	20.66, 19.68	1.30	1.52, 2.86	NTT1	lens, $z=1.505$
J0355-5624	58.8040	-56.4147	WD, MD	20.93, 20.03	1.29	—, 2.14	NTT1	lens, $z=1.86$
J0401-2514	60.4504	-25.2439	WD, MD	19.03, 20.22	1.45	1.67, 1.60	WHT	lens, $z=1.32$
J0405-3730	61.2721	-37.5128	WD	20.25, 20.57	1.70	0.58, 0.35	NTT2	lens, $z=3.585, z_{\text{lens}}=0.2295$
J0408+6333	62.2485	63.5522	WD	14.77, 16.89	0.99	3.19, 2.13	NOT	stars
J0416-5606	64.1783	-56.1073	WD, MD	20.08, 20.81	1.04	1.66, —	NTT1	lens, $z=1.45$
J0416+7428	64.1972	74.4827	WD	19.74, 19.02	2.64	1.96, 3.57	WHT	lens, $z=0.900, z_{\text{lens}}=0.097$
J0429-2246	67.4161	-22.7676	WD	17.42, 19.98	1.80	1.08, —	NTT2	galaxies, $z=0.206$
J0436+7851	69.1080	78.8530	WD, MD	19.00, 18.66	4.64	1.44, 0.82	NOT	projected QSOs, $z=0.765, 1.975$
J0440-0905	70.0482	-9.0911	WD, MD	19.92, 19.19	1.69	2.38, 2.15	WHT	lens, $z=2.105$
J0457-7820	74.3483	-78.3466	WT	19.60, 18.81, 19.07	4.89	1.12, 1.14, 1.50	NTT1	lens, $z=3.145$
J0504-2446	76.1616	-24.7752	GP	20.50, 19.22	2.05	1.48, 5.44	WHT	lens, $z=0.771$
J0526-3933	81.5470	-39.5630	WD	19.99, 20.69	1.41	1.88, —	NTT1	lens, $z=2.41$
J0527-2431	81.7608	-24.5328	WD	19.53, 20.57	1.46	2.60, —	NTT2	NIQ, $z=1.437$
J0544+4350	86.1448	43.8386	WD	19.64, 20.25	2.04	0.40, 1.09	WHT	lens, $z=3.11$
J0553+0910	88.2723	9.1812	WD, MD	19.71, 19.73	1.11	2.47, 2.63	NOT	projected QSOs, $z=1.08, 1.85$
J0601-2220	90.2664	-22.3464	WD, MD	20.65, 20.43	0.98	0.44, 2.12	NTT2	projected QSOs, $z=0.809, 0.836$
J0607-2152	91.7954	-21.8716	WT	20.86, 19.32, 20.90	1.57	—, 2.05, —	WHT	quad, $z=1.305$
J0608+4229	92.1725	42.4935	WT, MT	20.13, 18.23, 19.86	1.27	—, 3.94, —	WHT	quad, $z=2.346$
J0628-7448	97.2299	-74.8010	WD, MD	17.89, 20.50	2.61	2.27, 1.96	NTT2	lens, $z=2.692$

Table 1 – continued

Name	R.A.	Dec.	Selection	Gaia G	Sep. (")	Gaia P.M. sig.	Run	Classification
J0635+6452	98.9864	64.8715	WD, MD	20.86, 18.96	3.07	—, 0.55	WHT	lens, $z=1.845$ , $z_{\text{lens}}=0.427$
J0642+5337	100.7079	53.6284	WD, MD	19.74, 17.79	3.17	1.29, 1.31	NOT	NIQ, $z=1.86$
J0643+2725	100.9259	27.4276	WD	19.48, 19.82	2.44	0.88, 1.64	WHT	lens, $z=1.562$ , $z_{\text{lens}}=0.185$
J0659+1629	104.7667	16.4859	WT	18.59, 19.94, 20.05	5.25	1.73, 1.96, 0.78	WHT	quad, $z=3.09$
J0707+4109	106.9469	41.1640	WD, MD	20.53, 20.47	2.96	1.57, 1.30	WHT	QSO pair, $z=0.51, 0.516$
J0723+4739	110.9364	47.6529	WD, MD	20.36, 19.72	1.58	—, 2.42	NOT	NIQ, $z=0.842$
J0728+2607	112.1160	26.1173	WD, MD	18.92, 19.89	2.15	1.89, 0.38	NOT	NIQ, $z=1.025$
J0734+1915	113.6936	19.2501	WD, MD	18.10, 19.96	1.20	2.10, 0.49	NOT	lens, $z=0.745$
J0737+0925	114.3240	9.4298	WD, MD	19.90, 20.51	0.97	2.12, —	NTT4	$z=0.308$ QSO + star
J0740+0635	115.0907	6.5938	WD	19.56, 18.32	1.61	1.55, 1.84	WHT	lens, $z=1.78$
J0803+3908	120.9906	39.1398	WD, MD	18.88, 18.14	0.91	0.76, —	WHT	quad, $z=2.97$
J0805+3550	121.2733	35.8472	WD, MD	19.40, 19.93	1.13	3.62, 1.34	NOT	QSO pair, $z=1.66, 1.67$
J0816+2339	124.1428	23.6630	WD, MD	20.94, 20.32	1.99	—, 1.33	WHT	NIQ, $z=1.22$
J0818–2613	124.6179	-26.2237	WQ	19.74, 17.58, 19.94, 17.52	6.23	2.07, —, 2.01, —	WHT	quad, $z=2.155$
J0819+0457	124.8686	4.9522	WD	20.85, 20.58	1.84	—, 0.74	WHT	$z=0.456$ QSO + other
J0826+7002	126.5341	70.0456	GP	17.46, 19.30	5.83	1.06, 1.64	WHT	lens, $z=1.618$
J0833+0331	128.3369	3.5247	WD	20.08, 21.10	1.55	1.16, —	WHT	lens, $z=1.845$
J0833–0721	128.4731	-7.35185	WD, MD	19.45, 18.67	1.22	2.03, 1.65	NTT2	NIQ, $z=0.828$
J0833+2612	128.4767	26.2029	GP	20.93	1.79	—	NTT4	quad, $z=3.26$
J0834–2933	128.6411	-29.5505	WD	19.91, 20.17	1.80	2.96, 2.11	WHT	lens, $z=1.922$
J0839–0056	129.9448	-0.9371	GP	18.71	1.66	—	NTT4	$z=0.17$ galaxy + star
J0904+3343	136.1714	33.7291	WD	20.13, 19.93	1.50	4.06, 1.19	WHT	lens, $z=2.49$
J0907+6224	136.9660	62.4116	WD, MD	20.06, 19.27	2.49	1.45, 0.54	WHT	lens, $z=1.86$
J0909–0749	137.4946	-7.8179	WD, MD	18.24, 19.11	0.81	0.71, 1.13	NTT4	NIQ, $z=1.075$
J0911–0948	137.7845	-9.8054	GP	20.84	2.52	—	NTT3	lens, $z=1.47$ , $z_{\text{lens}}=0.251$
J0916–2848	139.1646	-28.8143	WD, MD	18.46, 19.47	1.01	1.88, 0.84	NTT2	NIQ, $z=1.925$
J0918–0220	139.6806	-2.3354	GP	20.43	2.26	—	WHT	lens, $z=0.803$ , $z_{\text{lens}}=0.460$
J0921+3020	140.2685	30.3421	MD	18.66, 20.85	2.93	1.40, —	WHT	lens, $z=3.335$ , $z_{\text{lens}}=0.428$
J0924+4235	141.1243	42.5947	MD	19.77, 20.70	4.64	0.90, —	WHT	lens, $z=3.17$ , $z_{\text{lens}}=0.415$
J0936–1211	144.2494	-12.1836	WD	17.49, 20.49	2.11	0.65, —	NTT2	lens, $z=2.00$ , $z_{\text{lens}}=0.260$
J0937+5835	144.3832	58.5906	WD	20.93, 20.45	1.44	—, 1.42	WHT	lens, $z=2.115$
J0938+0629	144.6502	6.4973	GP	19.21	1.15	—	NTT4	QSO+galaxy, $z=0.363$
J0939–0109	144.8548	-1.1636	GP	19.05	1.90	—	NTT4	QSO pair, $z=0.225$
J0941–2443	145.49455	-24.7308	WD, MD	20.48, 19.51	2.25	1.21, 1.69	NTT2	NIQ, $z=0.92$
J0947+0247	146.8048	2.7955	WD, MD	19.60, 20.54	1.49	1.04, —	NTT4	$z=0.643$ QSO + star
J0954–1421	148.7079	-14.3528	WD, MD	20.58, 19.80	1.40	—, 1.79	WHT	lens, $z=0.973$
J1003+0651	150.7886	6.8501	GP	19.85, 19.80, 20.20	2.62	0.84, —, —	WHT	lens, $z=2.565$ , $z_{\text{lens}}=0.225$
J1008+0046	152.1932	0.7724	WD, MD	20.60, 20.60	1.31	—, —	WHT	lens, $z=1.51$
J1008+0929	152.2041	9.4878	GP	19.01	1.76	—	WHT	lens, $z=3.08$
J1008–2911	152.2474	-29.1887	WD	20.41, 19.56	1.14	1.39, 1.12	NTT2	NIQ, $z=2.49$
J1019–1322	154.8066	-13.3692	WD	19.50, 20.44	1.14	0.18, —	NTT2	NIQ, $z=2.325$
J1019–3516	154.9803	-35.2742	WD	17.84, 19.99	1.76	1.44, —	NTT2	$z=0.136$ QSO + galaxy
J1025–2246	156.3567	-22.7690	WD	19.94, 21.31	3.92	0.20, —	WHT	lens, $z=1.97$
J1033–8249	158.4076	-82.8297	WD, MD	18.91, 20.27	2.33	0.57, 2.37	NTT2	NIQ, $z=1.69$
J1036–8544	159.1077	-85.7471	WD, MD	19.86, 19.73	1.22	1.56, 1.68	NTT2	NIQ, $z=1.09$
J1037+0018	159.3665	0.3057	WD, MD	19.95, 17.99	1.25	—, 2.46	NTT4	lens, $z=2.462$
J1041+1710	160.3081	17.1798	WD, MD	20.97, 19.49	1.62	—, 0.28	NTT4	lens, $z=2.01$
J1041–0836	160.3519	-8.6134	WD	17.81, 19.38	1.01	2.75, 0.76	NTT2	galaxy, $z=0.056$
J1045+3433	161.4977	34.5659	WD, MD	20.93, 20.38	1.42	—, 1.86	WHT	NIQ, $z=1.205$
J1102+3421	165.5267	34.3624	WD, MD	19.28, 19.63	1.25	2.28, 0.17	WHT	NIQ, $z=1.405$
J1103–1005	165.8665	-10.0940	WD, MD	17.79, 18.01	0.72	—, —	NTT2	NIQ, $z=1.292$
J1116–2122	169.1954	-21.3799	WD	18.44, 19.33	3.29	2.01, 0.40	NTT2	QSO pair, $z=0.709$
J1137–1245	174.3128	-12.7506	WD	20.78, 19.55	2.37	0.99, 0.52	WHT	lens, $z=2.18$
J1140+2303	175.0308	23.0637	WD, MD	20.19, 19.46	3.63	1.11, 2.12	NTT4	$z=2.405$ QSO + star(?)
J1144+1037	176.1344	10.6296	WD, MD	20.30, 19.69	1.00	3.64, 1.37	NTT4	$z=0.966$ QSO + star
J1202+0703	180.6182	7.0572	WD	19.76, 20.74	1.21	1.99, —	NTT4	NIQ, $z=2.187$
J1206–2543	181.7448	-25.7254	WD, MD	19.97, 20.40	2.08	1.27, 3.58	WHT	lens, $z=1.765$
J1209–1929	182.3615	-19.4879	WD	19.55, 20.66	1.46	0.89, —	WHT	lens, $z=2.91$
J1233–3542	188.3261	-35.7160	WD	19.56, 18.54	2.03	0.66, 1.26	WHT	lens, $z=2.28$
J1233–0227	188.4219	-2.4604	WD	19.74, 19.98	1.76	3.03, 2.91	WHT	lens, $z=1.598$ , $z_{\text{lens}}=0.345?$
J1237+3340	189.2537	33.6820	GP	20.90	1.57	—	WHT	lens, $z=1.795$ , $z_{\text{lens}}=0.35?$
J1247–3253	191.9855	-32.8919	WD, MD	19.09, 18.27	1.85	0.42, 2.01	NTT2	lens, $z=1.66$
J1255+0737	193.9324	7.6296	WD	20.40, 21.03	1.70	0.70, —	WHT	lens, $z=2.145$

**Table 1** – *continued*

Name	R.A.	Dec.	Selection	<i>Gaia</i> G	Sep. (″)	<i>Gaia</i> P.M. sig.	Run	Classification
J1303+1816	195.7765	18.2781	WD	20.20, 21.12	2.26	4.18, —	WHT	lens, $z=2.95$ , $z_{\text{lens}}=0.46$
J1307+0642	196.9290	6.7035	GP	20.16	3.51	—	WHT	lens, $z=2.03$ , $z_{\text{lens}}=0.230$
J1322+7852	200.7303	78.8791	WD	20.15, 20.20	3.59	0.46, —	WHT	$z=2.165$ QSO + gal $z=0.352$
J1326+3020	201.7410	30.3400	GP	20.24	2.11	—	WHT	lens, $z=1.852$ , $z_{\text{lens}}=0.339$
J1329–2807	202.4535	-28.1279	WD, MD	20.57, 19.23	1.90	—, 1.26	WHT	lens, $z=2.685$
J1344+6200	206.2040	62.0118	MD	20.14, 20.68	4.44	1.48, 0.65	WHT	lens, $z=2.21$
J1348+2925	207.2060	29.4195	WD, MD	18.43, 20.31	1.96	2.62, —	WHT	QSO+galaxy, $z=0.292$
J1350+3155	207.5956	31.9315	WD	18.89, 18.38	1.44	1.72, 2.91	WHT	$z=1.895$ QSO+ $z=0.211$ galaxy
J1408+0422	212.1406	4.3747	GP	20.61	2.59	—	WHT	lens, $z=3.005$
J1428+0500	217.2309	5.0058	WD, MD	19.89, 19.96	2.23	1.50, 2.26	WHT	NIQ, $z=1.375$
J1442–0857	220.7080	-8.9504	WD	18.96, 18.85	1.50	—, 1.78	NTT2	galaxies, $z=0.164$
J1449–2025	222.2960	-20.4276	WD, MD	18.65, 19.40	1.17	0.75, —	NTT2	NIQ, $z=0.594$
J1526–1400	231.6891	-14.0030	GP	19.29, 18.51, 19.35	2.65	1.00, —, —	WHT	lens, $z=0.648$ , $z_{\text{lens}}=0.096$
J1548–2914	237.1733	-29.2351	WD, MD	18.17, 20.07	1.99	0.70, 1.49	WHT	lens, $z=1.545$ , $z_{\text{lens}}=0.380$
J1550+0221	237.7387	2.3629	WD, MD	20.34, 18.44	2.03	0.42, 1.83	WHT	lens, $z=2.395$
J1652+4129	253.1935	41.4934	WD	20.10, 20.72	2.12	1.81, —	WHT	Galaxies, $z=0.217$
J1740+0311	265.1550	3.1966	WD, MD	19.50, 19.13	0.80	6.48, 0.94	NOT	$z=1.21$ QSO + star
J1752+0826	268.1779	8.4339	GP	20.54, 20.44	2.04	3.80, 4.55	WHT	$z=0.3195$ galaxy + stars
J1820+3747	275.1899	37.7879	WD	20.26, 17.93	3.10	1.44, 2.33	NOT	projected QSOs, $z=0.614, 0.754$
J1821+6005	275.3760	60.0908	WD, MD	20.33, 20.25	1.51	1.61, 2.27	NOT	NIQ, $z=2.052$
J1832+5349	278.1236	53.8206	WD, MD	19.58, 20.15	3.03	0.68, 2.06	NOT	NIQ, $z=1.160$
J1945–2857	296.3899	-28.9548	WD	19.94, 20.87	2.69	2.49, —	NTT1	lens, $z=2.56$
J2008+0438	302.0095	4.6433	WD, MD	20.01, 20.00	1.50	1.73, 2.34	NOT	NIQ(?), $z=1.70$
J2015+0707	303.8037	7.1171	WD, MD	20.72, 19.18	2.93	—, 0.18	NOT	lens, $z=2.59$
J2017+6204	304.4544	62.0787	WT, MT	19.15, 19.71, 20.14	0.92	4.05, —, —	NOT	quad, $z=1.73$
J2057+0217	314.4672	2.2967	WD, MD	20.14, 20.47	1.16	0.19, 0.62	NOT	NIQ, $z=1.52$
J2106–4944	316.5070	-49.7482	WD	20.86, 20.49	2.09	—, —	NTT1	lens, $z=1.296$ , $z_{\text{lens}}=0.290$
J2110–3755	317.5016	-37.9183	WD	20.97, 20.78	1.52	—, 1.79	NTT1	lens, $z=1.50$
J2121+1713	320.3801	17.2322	WD	17.99, 20.46	2.89	2.72, 1.57	NOT	QSO pair, $z=0.63$
J2124+2227	321.2344	22.4631	WD, MD	20.03, 20.01	0.90	—, —	NOT	$z=2.69$ QSO + star
J2132+3635	323.0301	36.5982	WD	19.95, 20.39	1.33	1.27, 1.51	NOT	NIQ, $z=1.215$
J2145+0039	326.4013	0.6661	GP	20.67, 19.96	2.08	—, 2.64	NTT1	$z=0.585$ QSO + star
J2147–1340	326.9957	-13.6772	WD	19.85, 20.23	1.33	1.87, —	NOT	lens, $z=1.382$
J2205+1019	331.4161	10.3307	WD, MD	18.53, 18.65	1.34	—, 1.69	NOT	lens, $z=1.78$
J2205–3727	331.4343	-37.4504	WD, MD	20.89, 20.57	0.76	—, —	NTT1	quad, $z=1.848$
J2212+0350	333.0713	3.8446	WD, MD	18.27, 20.57	0.94	1.77, —	NOT	$z=0.215$ QSO + gal or qso?
J2213–5926	333.3363	-59.4376	GP	20.83	2.59	—	NTT3 (NTT1)	lens, $z=1.72$
J2244–0550	341.0473	-5.8471	WD	18.23, 17.81	1.02	1.47, 1.09	NTT3	NIQ, $z=2.84$
J2255+8009	343.9088	80.1662	WD, MD	19.15, 18.86	0.74	2.02, 2.00	NOT	NIQ, $z=2.8(??)$
J2256+2223	344.0512	22.3943	WD, MD	20.68, 19.96	1.63	1.91, 0.67	NOT	QSO pair, $z=0.7515, 0.754$
J2302–4154	345.6308	-41.9157	WD, MD	20.27, 19.45	1.22	1.01, 2.24	NTT3	projected QSOs, $z=0.98, 1.22$
J2308+3201	347.0777	32.0294	WD	20.31, 19.54	2.63	1.41, 2.00	NOT	lens, $z=2.30$
J2311–1038	347.8207	-10.6472	WD, MD	20.56, 18.92	1.72	—, 2.09	NTT3	$z=1.53$ QSO + star
J2314+0323	348.5537	3.3929	WD, MD	19.30, 19.87	1.87	1.21, —	NOT	projected QSOs, $z=0.315, 0.606$
J2315+4857	348.7680	48.9532	WD, MD	19.92, 18.24	1.62	2.89, 1.64	NOT	$z=0.296$ QSO + star
J2316+0610	349.1335	6.1804	WD, MD	20.05, 20.75	2.32	1.18, —	NOT	lens, $z=1.955$
J2318+0250	349.5541	2.8411	WD, MD	19.59, 19.43	3.23	2.88, 0.78	NOT	projected QSOs, $z=1.83, 1.945$
J2322+0916	350.6413	9.2796	WD, MD	20.51, 18.18	4.51	1.50, 1.37	NOT	QSO pair, $z=1.20$
J2334+5036	353.5277	50.6114	WD	19.88, 19.18	2.13	1.99, 5.49	NOT	Stars
J2341–1557	355.4664	-15.9501	WD	20.71, 20.06	1.02	—, 0.85	NTT3	NIQ, $z=1.535$
J2355–4553	358.7761	-45.8931	WD	20.01, 20.69	2.20	1.67, 0.67	NTT3	QSO pair, $z=2.85$

Follow-up OSIRIS imaging reveals a third source closest to the Western image, which we take as a detection of the lensing galaxy (Figure 2).

#### 4.1.3 J0152-2448

This double system at  $z = 1.69$  was also independently discovered by Spiniello et al. (2019).

#### 4.1.4 J0200-1509

The EFOSC2 data shows a blended quasar spectrum at  $z=1.185$ . Given the two obvious *Gaia* detections and red residual flux upon subtraction of two PSFs in Legacy Survey imaging, which is well-fit by simultaneously including a Sersic which falls between the two PSFs, we designate this system as a lens.

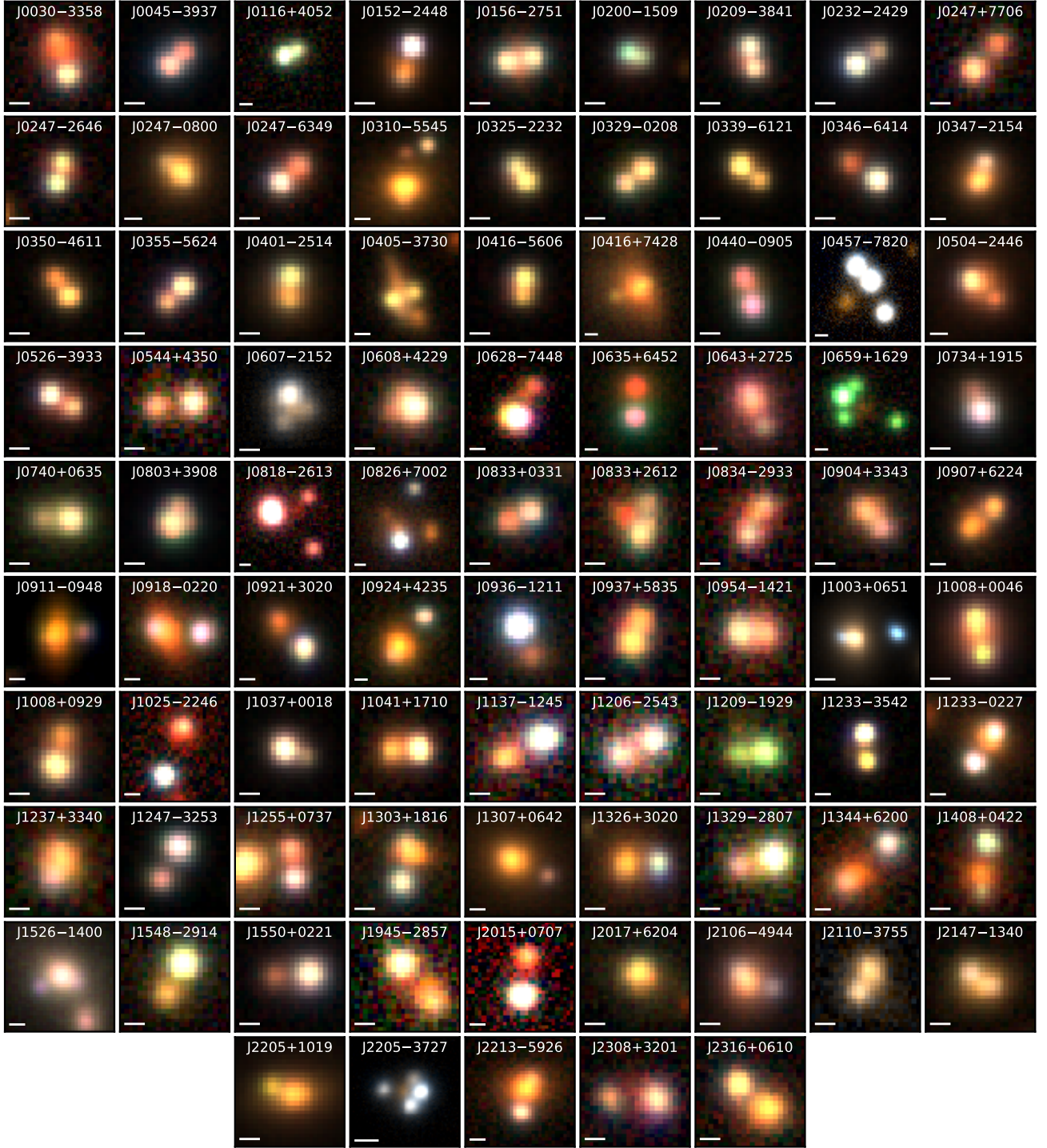


**Figure 1.** Colour images of the confirmed lensed quasars. HSC *gri*, Legacy Survey *grz*, and Pan-STARRS *gri* are used for the majority of the cutouts (with preference in the given order). Other imaging is shown as explained in the relevant system subsection of Section 4. White scale bars are  $1''$ . North is up, East is left.

#### 4.1.5 J0232-2429

This system was originally selected by [Lemon et al. \(2018\)](#), who classified it as a likely quasar+star projection, despite poor seeing during observations and the small separation of  $1.44''$ . However, we obtained further spectroscopy to confirm this classification, and resolve two quasars at  $z = 1.58$  with similar emission line profiles

and continuum. There is residual red flux in the PSF-subtracted Legacy Survey image, consistent with a lensing galaxy. We therefore upgrade the classification to a secure lens. The system is in the outskirts of a cluster ( $\sim 1'$  from the centre) which has galaxies with photometric redshifts of  $\sim 0.85$ . The quasar is radio loud with

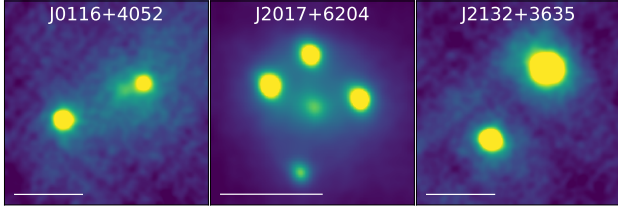


**Figure 2.** OSIRIS imaging of three systems. White scale bars represent 1 arcsecond. North is up, East is left. Galaxies can be seen between the quasar images for J0116+4052 ( $z = 1.85$ ) and J2017+6204 ( $z = 1.73$ ), however nothing is seen for J2132+3635 ( $z = 1.215$ ), therefore it is likely a physical binary.

detections in NVSS ( $4.7 \pm 0.7$  mJy at 1.4GHz) and VLASS ( $2.7 \pm 0.4$  mJy at 2–4GHz).

#### 4.1.6 J0247+7706

The ALFOSC-NOT spectra clearly resolve two quasar traces at  $z=2.73$  and many narrow absorption lines common to both components. Faint hints of an extended galaxy are seen in the PSF subtracted Pan-STARRS imaging. When adding a Sersic component to the fit, flux is allocated in all bands to this component, and its best-fit position is between the two PSFs closer to the fainter image. Given this and the very similar spectra, we classify this system as a lens, however deeper imaging should be taken to verify the detection of the lensing galaxy and characterise its properties.

#### 4.1.7 J0247-6349

The seeing for this spectrum was particularly poor, leading to low signal-to-noise and a blended spectrum. The 2D spectral modelling allocates emission line flux to both components, however cannot be taken as reliable. Nevertheless, the emission lines are clearly from a  $z=2.295$  quasar, and the Legacy Survey images show two point sources either side of a red galaxy. Therefore we classify this system as a lens. This is supported by the independent spectra and discovery of this system by Spiniello et al. (2019).

#### 4.1.8 J0310-5545

This double was selected as a single *Gaia* detection near a possible LRG, however the *Gaia* detection is not associated to one of the quasar images but to a nearby star. The possibility of two further point sources around the nearby galaxy was noticed serendipitously during visual inspection. Deep EFOSC2-NTT spectra aligned to capture the galaxy and two faint sources clearly show three traces, two of which contain emission lines of a quasar at  $z=2.31$ , and the middle trace being an LRG at  $z=0.298$ , therefore confirming this system as a lensed quasar.

#### 4.1.9 J0325-2232

The spectra show emission lines of a  $z=1.35$  quasar in both components, however the continua and relative emission line amplitudes are clearly discrepant, with stronger broad emission lines in the redder image. Legacy Survey imaging shows a galaxy between the two components, which is well fit by a Sersic positioned between the PSFs and slightly nearer the South-Western image, B. In the *g*-band of both Pan-STARRS and Legacy Survey imaging, A is brighter

than B, however B is brighter in both *Gaia* (by 0.21 mag in the broad *G* filter) and in the ground-based red filters, even when including the galaxy in the fit. Absorption is present around  $4785\text{\AA}$  and  $4890\text{\AA}$  in only the redder image. This system is likely a lens with contamination and reddening by the lensing galaxy coupled with microlensing. Deeper spectra will be useful for understanding the nature of the discrepant spectra.

#### 4.1.10 J0329-0208

This double lensed quasar lies  $3.5'$  from the centre of the cluster MACS J0329-0211. The *HST* coverage of the cluster narrowly misses this lens system, however *Chandra* ACIS-I imaging does cover the system, revealing an extended X-ray source with a measured flux of  $4.11 \times 10^{-14}$  erg cm $^{-2}$  s $^{-1}$  in the 0.3–8 keV range (Wang et al. 2016). The lensing galaxy may be a member of this  $z=0.45$  galaxy cluster, however there are no obvious absorption lines in our spectra around this redshift.

#### 4.1.11 J0339-6121

This double shows signs of a LoBAL quasar source at  $z \approx 1.89$ , with the troughs blueshifted by around 0.028c, typical of many BAL quasars (Rankine et al. 2020). While the absorption around  $5762\text{\AA}$  could be attributed to FeIII-UV48 triplet, it is more likely to be due to the CrII-2062 $\text{\AA}$  triplet since we do not see strong evidence for the defining FeLoBAL FeII UV1 and UV2 lines. The flux ratio of the images across wavelength is approximately constant (2.4:1) but shows clear differences around several absorption lines, suggesting microlensing is present in the system, a particularly useful tool for constraining the quasar source geometry (Hutsemekers et al. 2010; Sluse et al. 2015).

#### 4.1.12 J0350-4611

The NTT-EFOSC2 spectra of this double are low signal-to-noise but each component shows emission lines of a  $z=1.505$  quasar. The CIV profile is not apparent, and there is a significant drop in flux at the expected wavelength and blueward of CIV in both components. The lens is seen in the Legacy Survey PSF-subtracted residuals. Deeper spectra should be taken to understand the nature of this system, as it is possibly a useful lensed BAL quasar.

#### 4.1.13 J0405-3730

The 2D spectra of this double show the resolved traces of the images of a quasar at  $z=3.585$ , but also three narrow emission lines located between the two quasar traces, but much closer to the brighter trace. These lines are consistent with OII, H $\alpha$  and SII at  $z=0.2295$ , and a narrow absorption line in the brighter trace can also be attributed to Na at this redshift. The imaging of this system shows that at least two galaxies are responsible for the lensing, one between the two images but offset and highly elliptical and another offset. We postulate that the lens is a merger between two galaxies, triggering star formation explaining the aforementioned narrow lines. High-resolution imaging will be needed to better understand this system.

#### 4.1.14 J0416+7428

This double has a very low redshift lens ( $z=0.098$ ), which appears to be part of a group with two nearby galaxies apparent in the Pan-



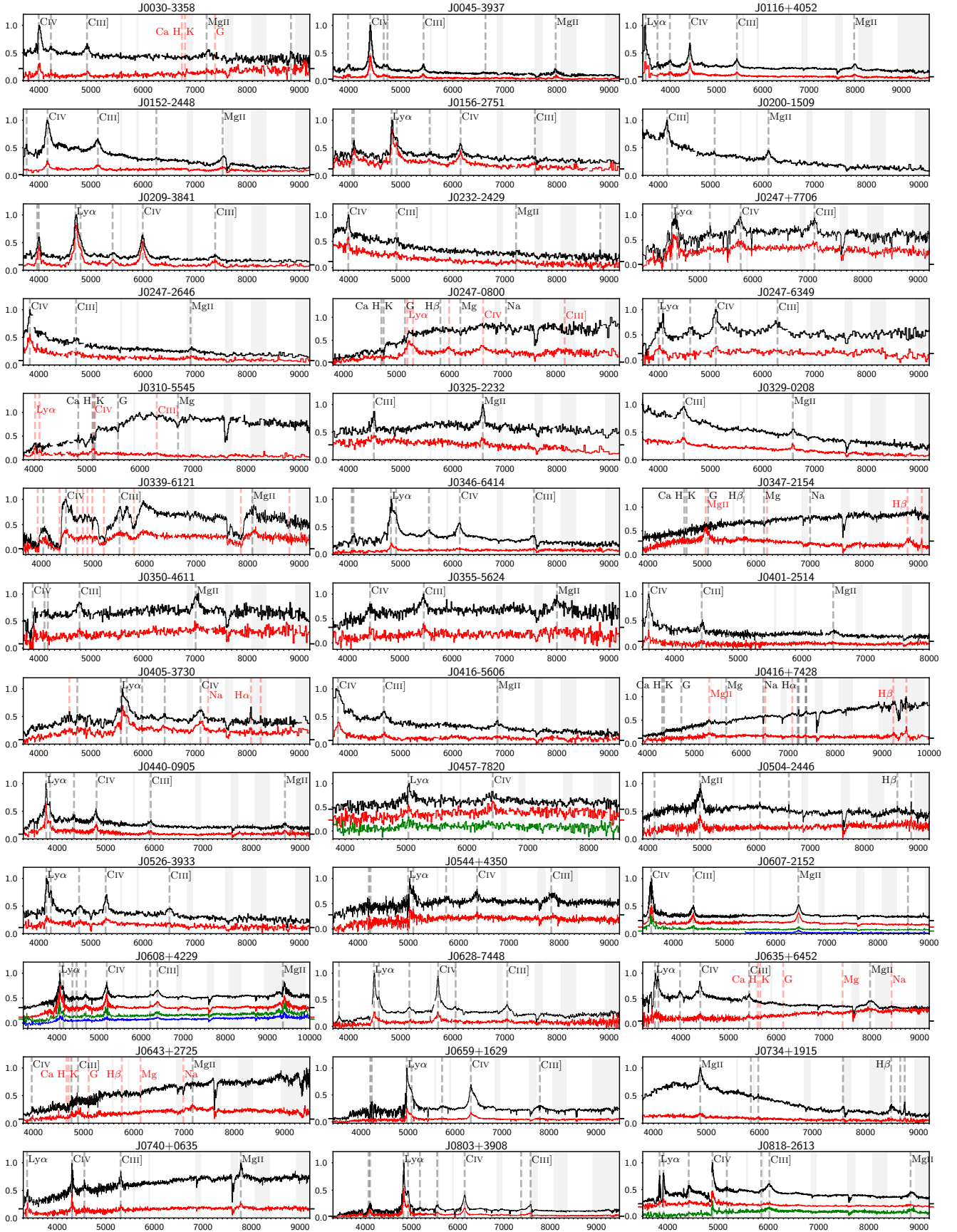


**Figure 3.** Spectra of the confirmed lenses in the observed frame. The most prominent quasar emission lines are marked with vertical lines, and details on certain spectra can be found in Section 4. In some cases one or several spectra have been offset for visualisation, and the offset is marked on the y-axis.

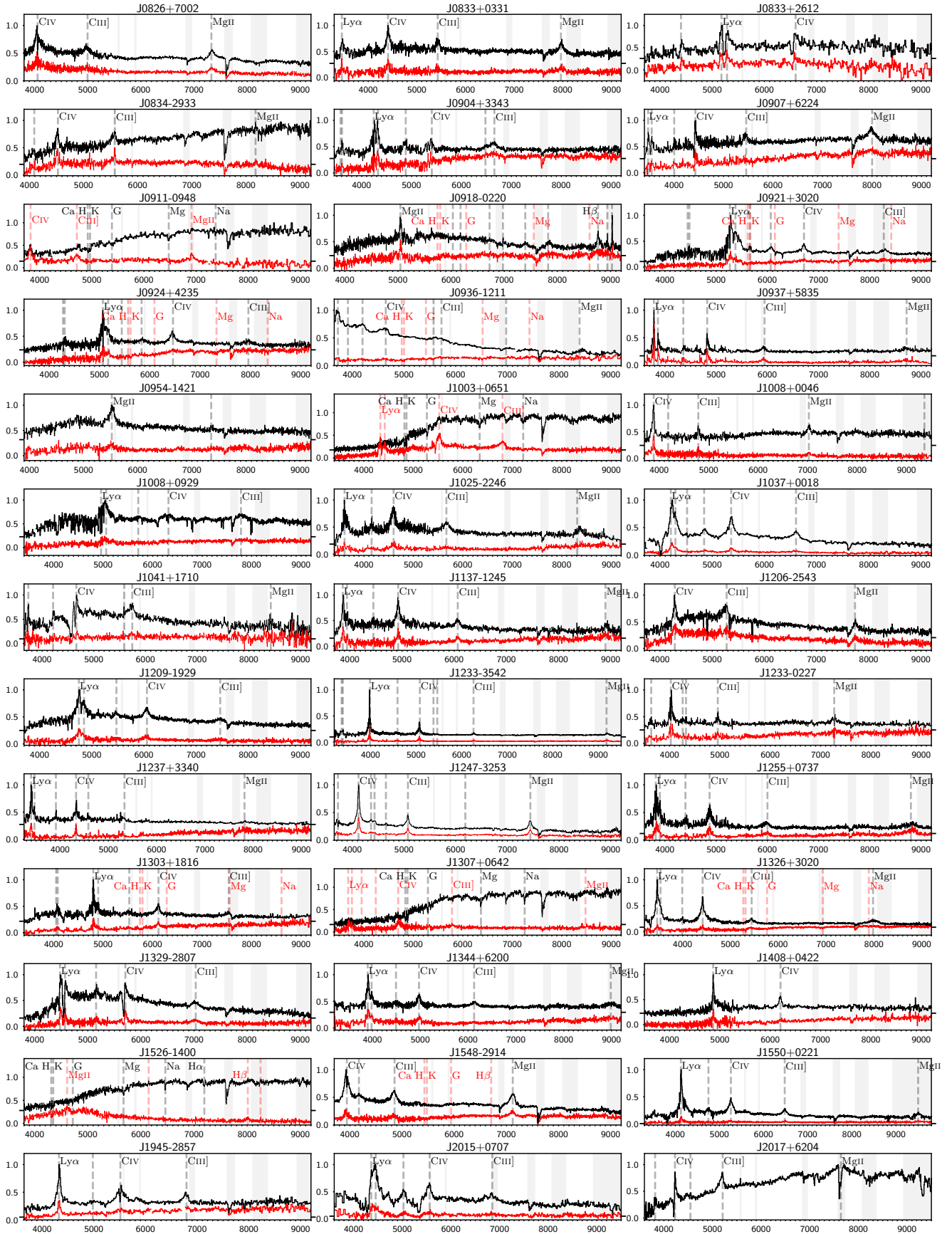


Figure 3 – continued

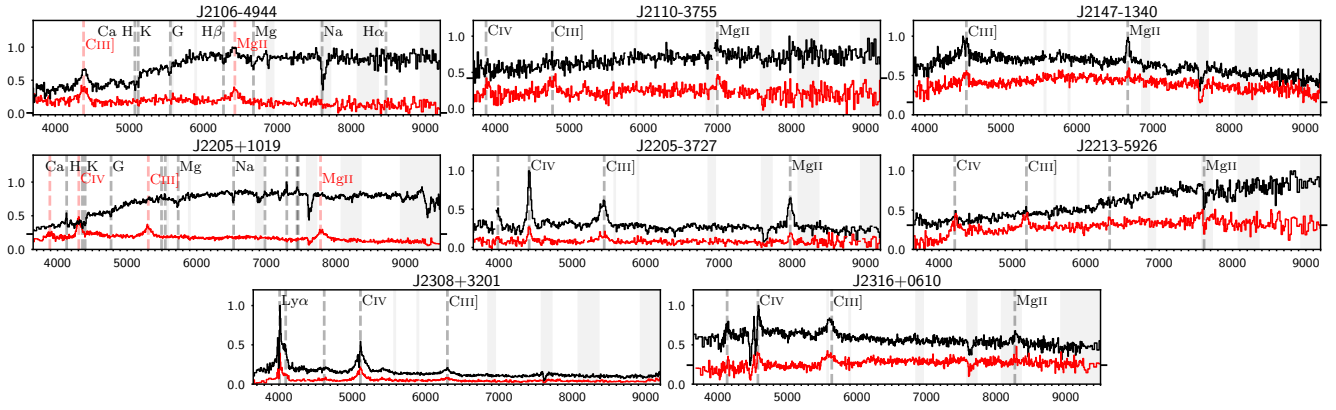


Figure 3 – continued

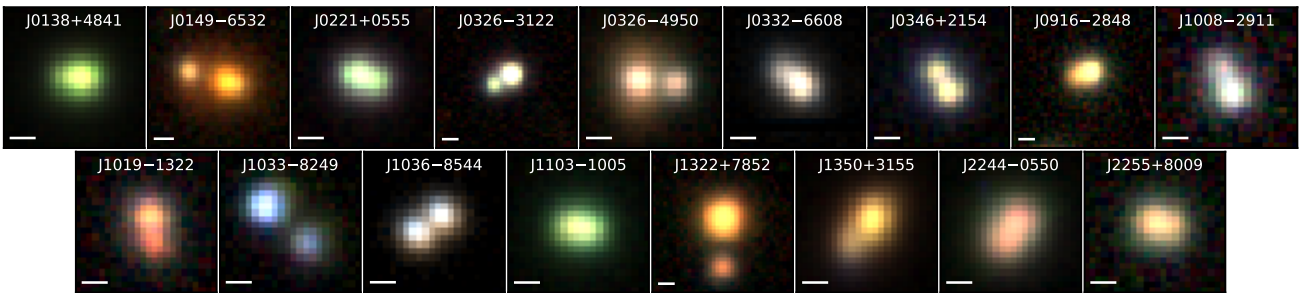


Figure 4. Colour images of the probable lensed quasars, requiring deeper imaging or spectra. Scalebars are 1 arcsecond.

STARRS imaging. In the 2D spectra, narrow emission lines are seen both 4.6 arcseconds from the main lensing galaxy in the direction of the more distant image, and also 13 arcseconds in the other direction coincident with diffuse extended continuum emission for the latter. These lines are consistent with  $H\alpha$  and  $N\text{II}$  emission at the lens galaxy redshift, therefore we attribute the former to a star-forming region in the outskirts of the main lensing galaxy, and the latter to star formation in the outskirts of the galaxy group member to the West. The lensing galaxy has an  $i$ -band brightness of 16.22. The low redshift of the lensing galaxy is rare amongst lensed quasars, with the only known lensed quasar with a redshift lower than this being the Einstein cross (Huchra et al. 1985). Another double in our sample, J1526-1400, also has a low-redshift, bright lensing galaxy, so we investigate the expected number of lenses as a function of lensing galaxy brightness after describing J1526-1400 in Section 4.1.42.

#### 4.1.15 J0457-7820

This system was selected through the *Gaia* multiplet WISE search, with three *Gaia* detections ( $G=18.81, 19.07, \text{ and } 19.60$ ) and  $W1-W2=0.95$ . Archival NOAO DeCAM imaging shows three bright blue point sources around a galaxy. The follow-up NTT-EFOSC2 spectra, positioned to capture light from all three images simultaneously, are low signal-to-noise but clearly show three traces of a  $z=3.145$  quasar. Three  $g$ -band and three  $i$ -band exposures, each of 120s were taken with the Magellan Instant Camera, MagIC. A second galaxy is apparent to the North-West of the system. All six exposures were fit simultaneously as two galaxies and three point

spread functions, with the PSF being fit as a grid of pixels, and constrained directly from the data (following Ostrovski et al. 2018). Figure 10 shows the colour-image stack (where the green channel is a median of the  $g$  and  $i$  bands), and residuals. No counterimage is detected. We repeat the image subtraction but artificially include a point source of increasing brightness until it is obvious in the residuals. This provides an upper limit on any counterimage brightness being 1% as bright as image B, i.e. a  $G$ -band magnitude of  $\sim 24.0$ . One possibility is that this is a rare three image system caused by the straddling of two galaxies. Shin & Evans (2008) provide a comprehensive catalogue of image configurations caused by lensing of two separated galaxies, modelled as Singular Isothermal Spheres. Several configurations allow for three image regions within the resulting caustics, where the third image is not necessarily strongly demagnified. Given that all images lie between the two galaxies, the most likely configuration is 3B-1, following the labelling of Shin & Evans (2008). This naked catastrophe occurs when the two astroid caustics merge in a beak-to-beak calamity (see, e.g., Kassiola et al. 1992; Orban de Xivry & Marshall 2009), but the pseudo-caustics do not overlap, creating a naked merged cusp region. Introducing external shear and mass ellipticity can create naked cusps which are not necessarily merged, again creating source plane regions corresponding to three bright images.

To test which is the relevant scenario for J0457-7820, we perform mass models based on the astrometry from fitting the MagIC imaging. We use only the positions to constrain the mass model, since microlensing, extinction, and variability over the time delay can cause optical image fluxes to vary significantly from their macromodel values. This gives us only 6 free parameters. A single SIE model fixed to the main lensing galaxy, predicts a fourth image,

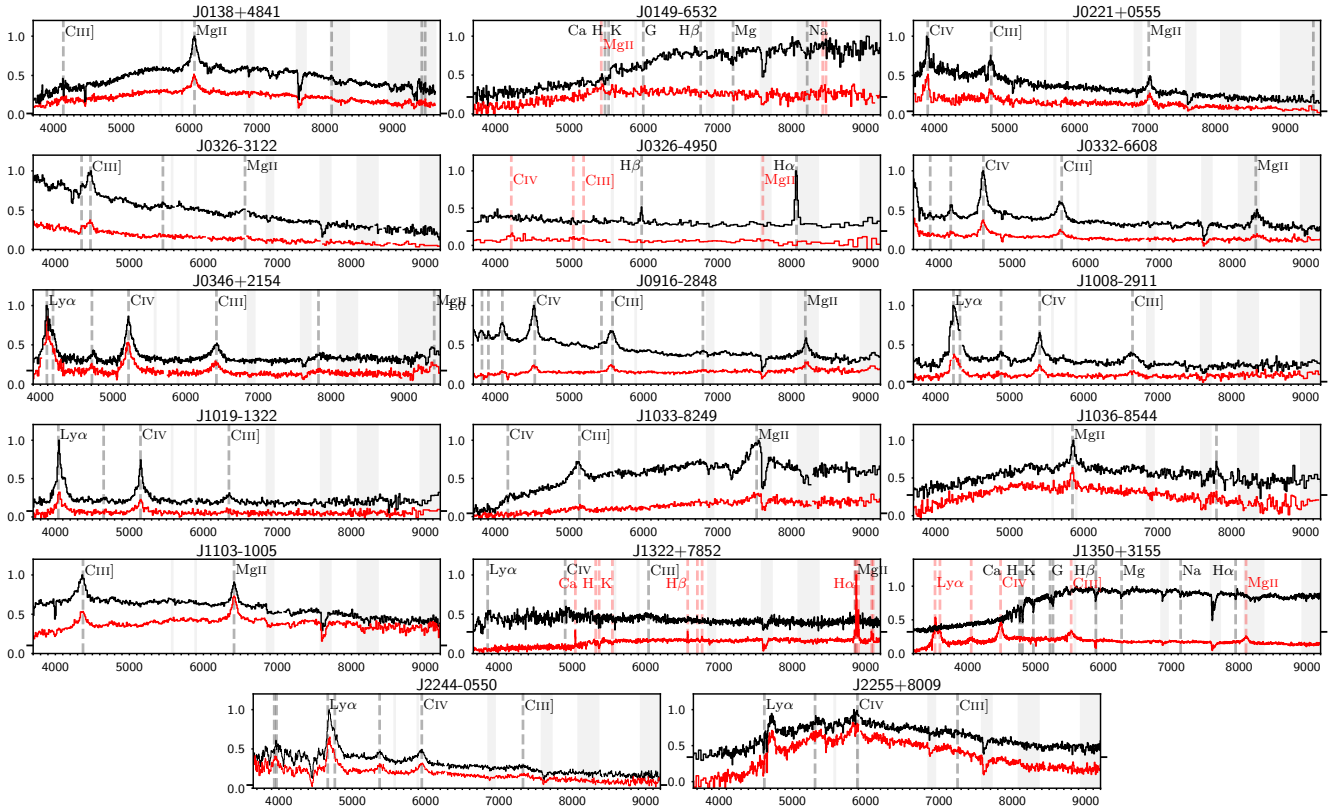


Figure 5. Spectra of very likely lensed quasars. Details of the spectra are explained in Figure 3.

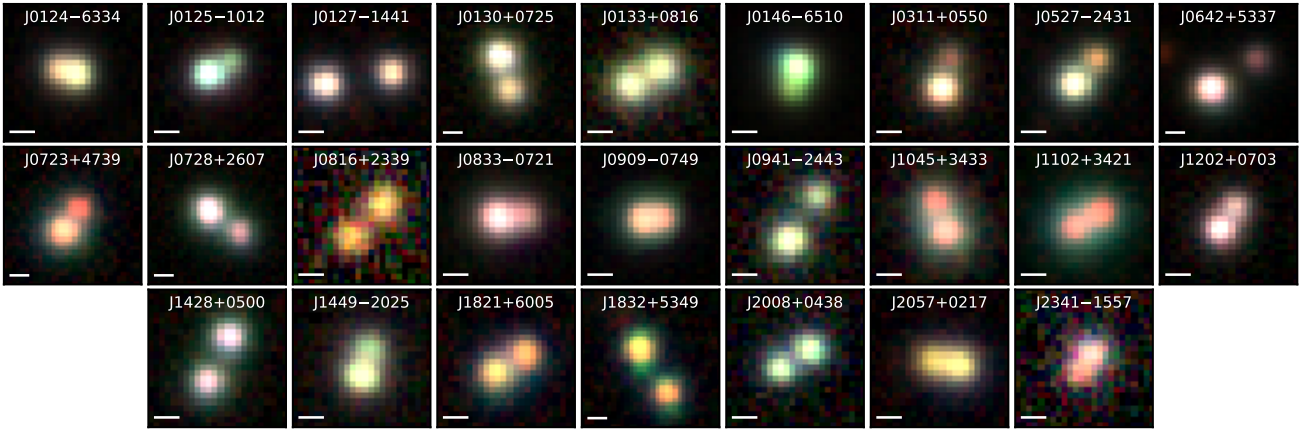
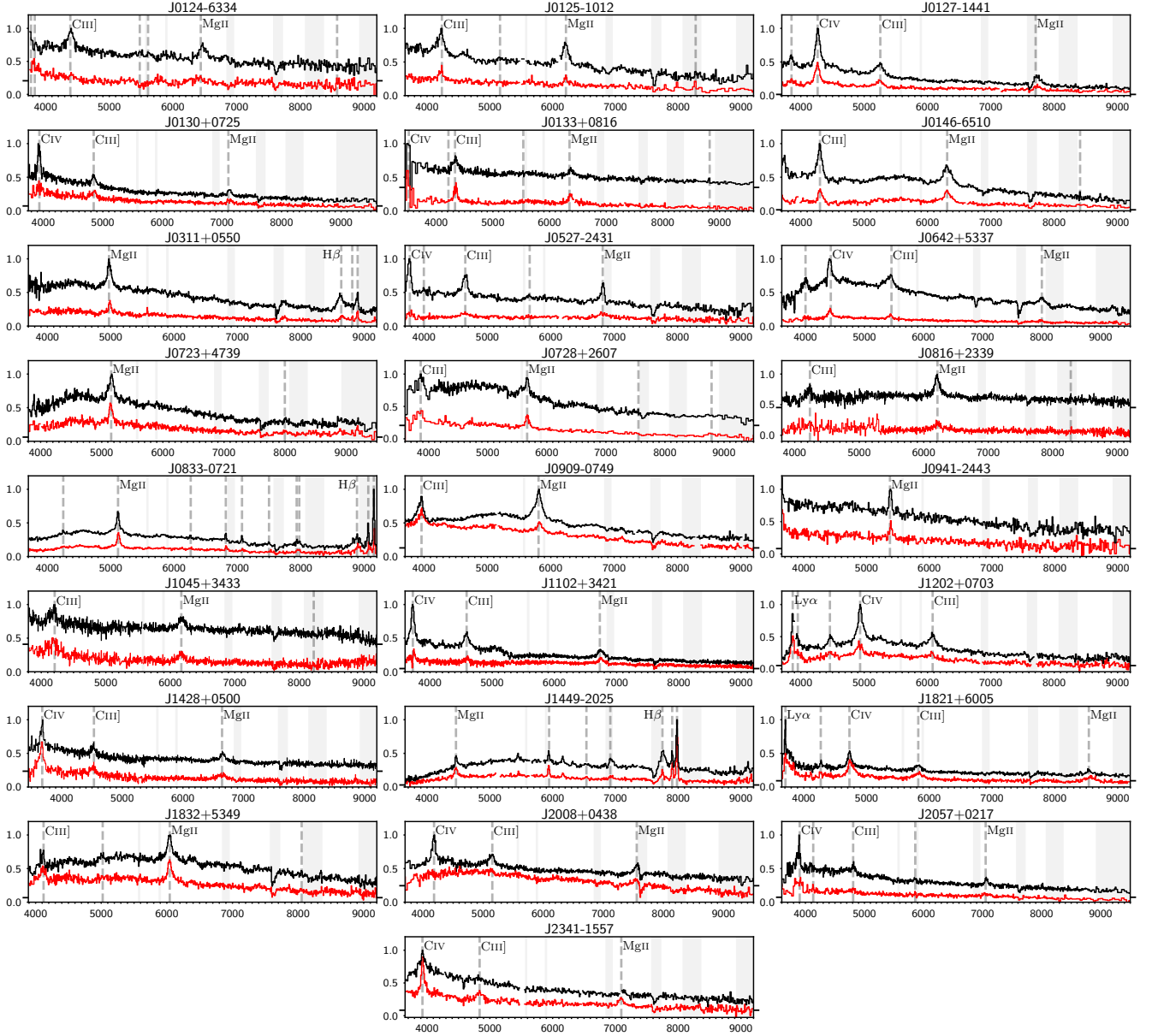


Figure 6. Colour images of the unclassified quasar pairs.

only 2.5% the brightness of B. Such an image could be consistent with our 1% detection threshold coupled with reddening and microlensing demagnifying such an image, however, the model is unphysical with an axis ratio of 0.2, and the image positions are not well recovered. Including shear in the model recovers the image positions exactly, but also predicts a fourth image, about 1% as bright as B. The lensing galaxy mass is also less elliptical (0.14) but a large shear of 0.35 is required, in the direction of the second galaxy. We note that this model has more free parameters than constraints, however some parameters are still well-constrained. This model can

be forced to have three images with very little change in the mass model parameters and well-fit images ( $\chi^2 \sim 0.4$ ). Given the shear direction, we investigate two component mass models. SIS+SIS or SIS+SIE models do not recover the three image positions. An SIE+SIE model fits the images and does not predict a fourth image, however the galaxies are predicted to have large ellipticities and lie in the same direction ( $\sim 25$  degrees North of West). Adding shear to this model reduces the ellipticities of the mass components and still recovers only three images, however, the lens parameters are not as well constrained. We show the caustics of this best-fit model



**Figure 7.** Spectra of unclassified quasar pairs. Details of the spectra are explained in Figure 3.

in Figure 10. In this instance the cusps do not merge, but since the model is still under-constrained further constraints from the lensed source host galaxy (and limits on a possible fourth image) will be needed to determine more reliable caustic configurations.

#### 4.1.16 J0607-2152

This quad was confirmed during the 2019 WHT observing run, in which the system was targeted at two position angles: through the brightest image and each of the other two *Gaia* detections. The traces are resolved in the red arm, however in the blue arm of one observation, the images are not resolved, hence we show only the red arm extraction for the fainter image in Figure 3. The extracted fluxes for the brightest image between the two exposures are in good agreement in the red arm, however in the blue arm they are in disagreement likely due to slit losses and blending. Figure 11

shows the presence of two further objects between and to the East of the 3 *Gaia* detections. Including a galaxy and a further PSF fits the data to the noise, so we expect that these are the lensing galaxy and fourth quasar image. Using these 5 positions, we are not able to fit an SIE+shear model to the data, suggesting a more complex lensing model is required, or the fourth image is much closer to A. This system was also independently confirmed by Stern et al. (2021). They suggest that the fourth image is between the Northern components, however this is not supported by the aforementioned residuals.

#### 4.1.17 J0608+4229

This system has three *Gaia* detections with  $G=18.22, 19.86, 20.12$ . It was confirmed during the Feb 2019 WHT observing run, in which the system was targeted at two position angles: both through the

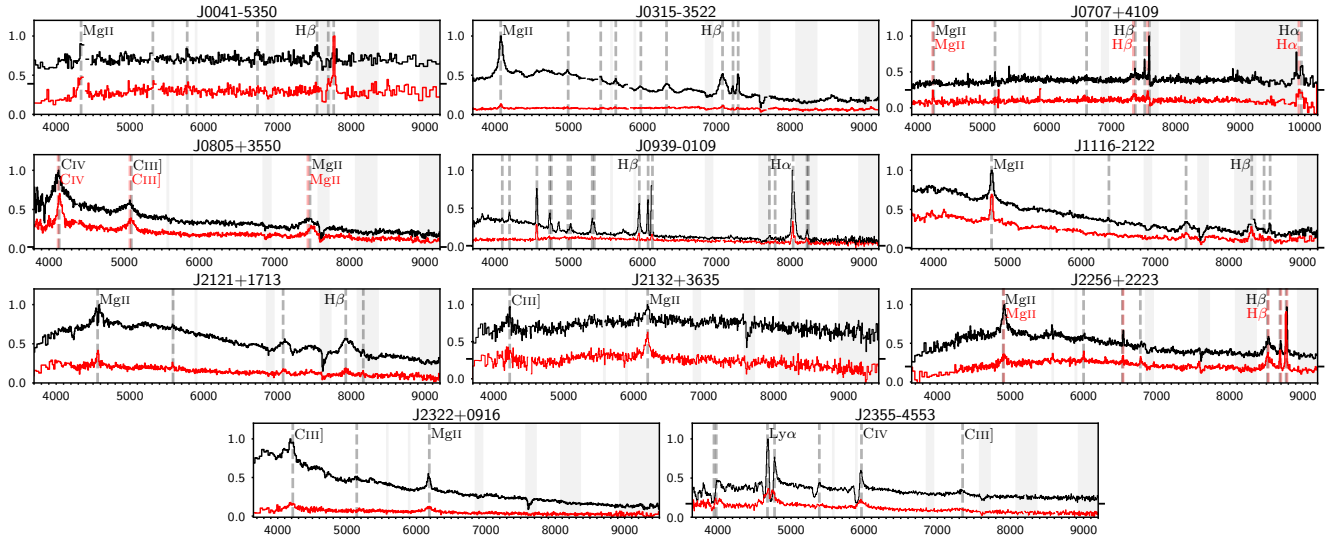


**Figure 8.** Spectra of binary quasars, with strong evidence for being distinct, and thus not gravitationally lensed. Details of the spectra are explained in Figure 3.

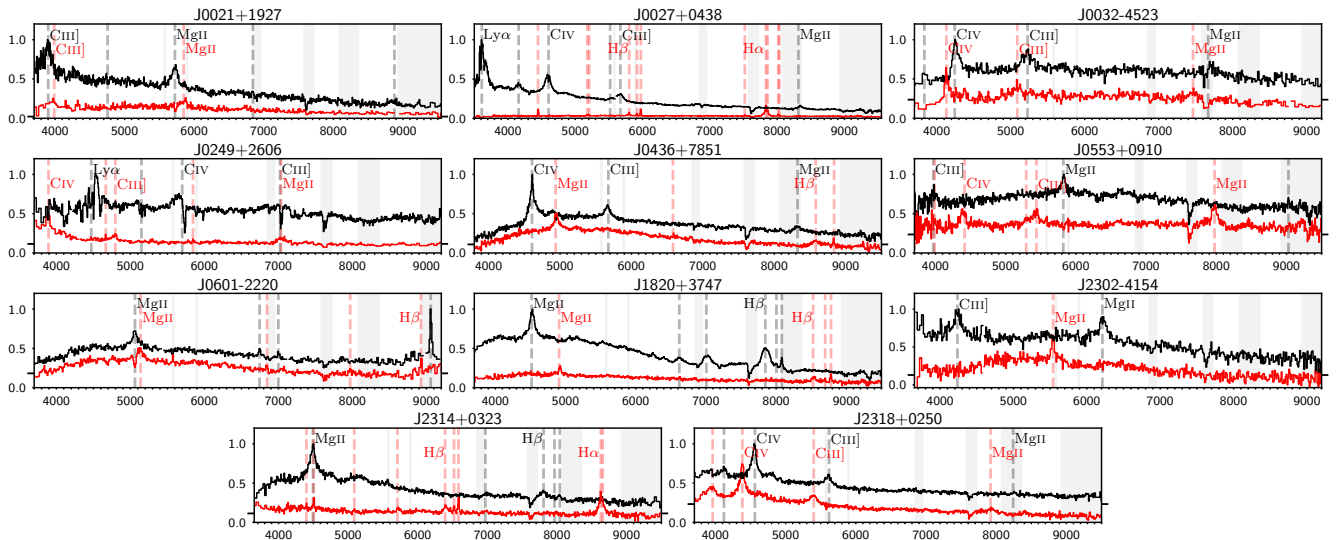


**Figure 9.** Spectra of projected quasar pairs. Details of the spectra are explained in Figure 3.

brightest *Gaia* detection and each of the other two detections. The forced fitting extracts very similar spectra for each component. The multiple extractions of the brightest image are in good agreement, with only a slight mismatch in the relative amplitudes in the red arm, likely due to the flux-matching procedure of the blue and red arm spectra. Modelling the system as three PSFs reveals residual flux just south of the brightest image, and modelling the systems as four PSFs fit the Pan-STARRS data to the noise, as shown in Figure 12. We note, however, that no lensing galaxy is seen upon PSF subtraction, but this is often expected to be the case for higher redshift sources (here,  $z=2.34$ ). An SIE model fit to the four image positions shows A is observed brighter than the model, and D is observed fainter. Since D is a saddle point in this model, microlensing could be the cause of its relative demagnification (Schechter & Wambsganss 2002). This system was also independently confirmed by Stern et al. (2021).

#### 4.1.18 J0628-7448

Archival DECam data of this system reveal significant residuals after subtracting two PSFs, and flux is seen in the residual 2D NTT-EFOSC2 spectra towards redder wavelengths. Given also the similarity of the spectra, we classify this system as a lens. The system is associated with an XMM Slew Survey catalogue detection with a flux of  $1.6 \pm 0.8 \times 10^{-12}$  erg cm $^{-2}$  s $^{-1}$  in the 0.2–12keV band.

#### 4.1.19 J0635+6452

This is a large flux-ratio, 3.06''-separation double. The Pan-STARRS *gri* data appear consistent with only a PSF+galaxy, however a *Gaia* detection associated with the galaxy suggested the presence of a counterimage, which our WHT spectrum confirms. The fainter image has dropped from  $G=20.57$  to  $G=20.86$  between GDR1 and GDR2.

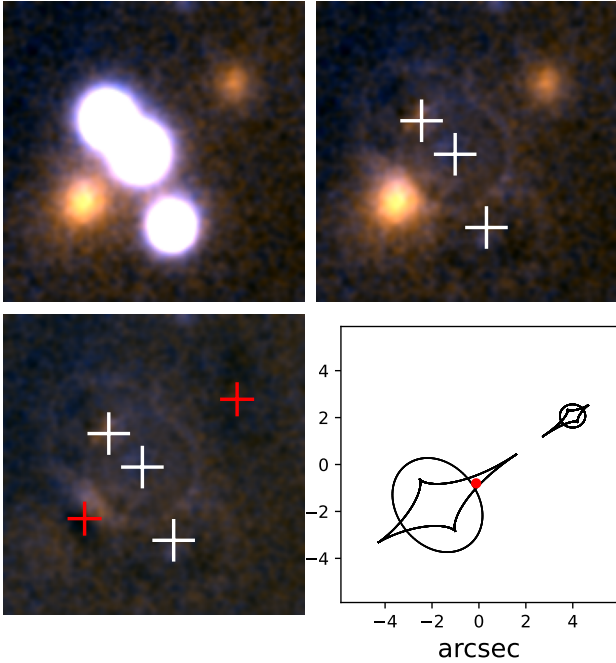


**Figure 10.** (a) MagIC *g* and *i*-band imaging of J0457-7820; (b) with a 3 PSF model subtracted, (c) with galaxies and PSFs subtracted, (d) fiducial mass model caustics with source position overlaid (see text for details).

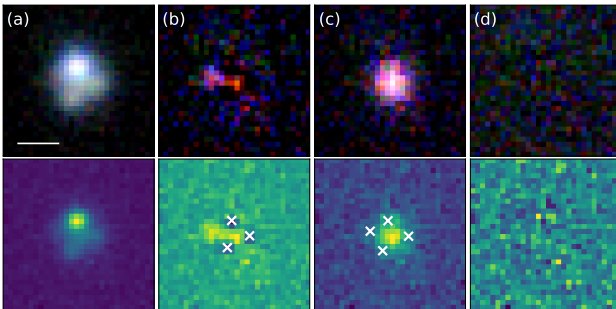


**Figure 11.** Analysis of Pan-STARRS imaging of J0607-2152. Top row is for *gri*, while the bottom is just *r*-band. (a) original data, (b) with a 3 PSF model subtracted, (c) with 4 PSFs subtracted from a 4 PSF + galaxy model, (d) residuals of the 4 PSF + galaxy model.

#### 4.1.20 J0643+2725

This double has a bright lensing galaxy at  $z=0.185$ . In the Pan-STARRS imaging, the quasar image closest to the lensing galaxy is the brightest (and is likely resolved since the *Gaia* astrometric excess noise — a catalogue parameter correlating with extendedness — is 2.57, a small value compared to most galaxies).

#### 4.1.21 J0659+1629

This lens is a short axis quad, with a large Einstein radius,  $\sim 2.3''$ . We obtained spectra of the two brightest images, confirming the source to be a quasar at  $z=3.09$ . The best fit SIE+shear model has a magnification of 25, and a modest shear of 0.06. The model predicts image D to be 60% fainter than observed. Since this system has a large time delay between image D, we expect that variability over the time delay can explain this discrepancy. This system was

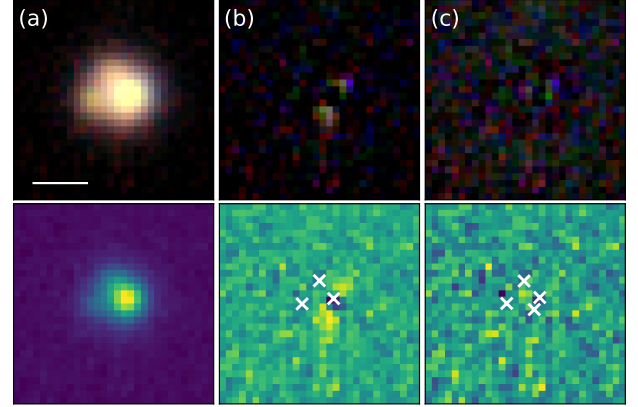


**Figure 12.** Analysis of Pan-STARRS imaging of J0608+4229. Top row is for *gri*, while the bottom is just *r*-band. (a) original data, (b) with a 3 PSF model subtracted, (c) with a 4 PSF model subtracted.

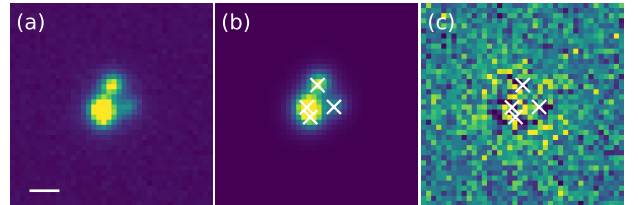


**Figure 13.** (a) CFHT *r*-band image of J0803+3908 with a  $1''$  scalebar, (b) model with PSF positions overlaid, (c) residual image possibly showing extended emission from the lensing galaxy.

also independently selected by [Delchambre et al. \(2019\)](#) as a lens candidate, and independently confirmed by [Stern et al. \(2021\)](#).

#### 4.1.22 J0734+1915

The 2D spectrum shows the traces of two quasars at  $z=0.745$  however the signal to noise of the fainter quasar is low, making comparison difficult. Both Legacy Survey and Pan-STARRS imaging reveal significant residuals in the PSF-subtracted image, which are well fit when including a galaxy which falls between the two PSFs but closer to the fainter one. We classify this system as a lens, however we suggest prioritising high-resolution imaging or deeper spectroscopy of this system to verify the lensing hypothesis.

#### 4.1.23 J0803+3908

This system was originally selected with the unWISE modelling technique, given it has two *Gaia* detections separated by  $0.91''$ . Good-seeing CFHT *r*-band data reveal a fold configuration quad. Figure 13 shows these data, with a 4 PSF fit and subtraction, showing faint extended residuals possibly due to a lensing galaxy. Very good seeing conditions allowed spatially resolved spectra between the bright pair and the Northern image, confirming the source to be at  $z=2.97$ . [Schindler et al. \(2018\)](#) confirmed this source as a bright quasar at  $z=2.975$  in their North Galactic Cap sample of the Extremely Luminous Quasar Survey (ELQS-N), however they did not comment on any possibility of it being gravitationally lensed. Such catalogues present a good opportunity for finding compact lensed quasars thanks to the magnification bias of lensing.

## 4.1.24 J0818-2613

This system was confirmed during the 2019 WHT observations. It was discovered as four *Gaia* detections associated with a red ALLWISE detection. Spectra were taken at two position angles, each through the bright pair, and clearly show that the source is a  $z=2.155$  BAL quasar with multiple velocity outflows (e.g., Korista et al. 1993). The system is in a high stellar density environment, since it is at a galactic latitude of  $+5.4^\circ$ , an area which has been purposefully omitted from previous searches due to high contamination rates. The strong constraints from requiring four *Gaia* detections around photometric quasars allows us to now probe such high-density regions. The *Gaia* magnitudes are 17.51, 17.58, 19.73, and 19.94, and the system has 3 ROSAT counts within  $25''$ . The system was targeted for spectroscopic follow-up despite the high stellar density and odd configuration, since the SEDs from optical to infrared wavelengths for all images are similar, and a faint lensing galaxy is seen upon subtraction of the PSFs. The image configuration is peculiar for a quad. When fitting an SIE+shear model to the 4 image positions and relative fluxes, the lensing galaxy position is recovered to within  $0.5''$ . A model using the galaxy position provides a total magnification of 58, a galaxy mass ellipticity of 0.61, and position angle 34 degrees East of North, with a strong shear of 0.38 at a position angle 126 degrees East of North. This model seems highly unphysical with such a large shear and orthogonal mass and shear axis directions, and is perhaps indicative of the lensing potential not being simple. Indeed, the large Einstein radius of  $2.96''$  is suggestive of a galaxy group or cluster acting as the lens. The lens was also independently confirmed by Stern et al. (2021).

## 4.1.25 J0826+7002

The system was originally targeted in a GDR1 search (Lemon et al. 2018), as it was selected as a *Gaia* singlet near a morphological Pan-STARRS galaxy, however the WHT spectra were not deep enough to confirm the fainter object as a quasar. It was targeted again after it was recovered by the same search technique in GDR2, and better seeing conditions and lower airmass observations reveal both *Gaia* detections to be quasars at  $z=1.62$ . Both images are detected in GDR1 and GDR2, but the separation is  $5.82''$ , hence the system was not discovered by the unWISE modelling or WISE-*Gaia* doublet selection. Pixel modelling shows three lensing galaxies lying closer to the brighter image. There is a third *Gaia* detection in *Gaia* EDR3 on the Western galaxy of these three, perhaps hinting at a third image of the quasar blended with the galaxy. High-resolution imaging is needed for this system.

## 4.1.26 J0833+2612

This lens was selected as a single *Gaia* detection offset from a Pan-STARRS morphological galaxy (Section 2.3). The slit was positioned at  $167.4$  degrees East of North, and clearly resolves two traces of a BAL quasar at  $z\approx 3.26$ . The DECALS residual imaging shows a likely faint counterimage, confirming this system as a quad. CFHT  $r$ - and  $z$ -band imaging also show a counterimage, and our PSF-subtracted modelling of these data is shown in Figure 14. There is a coincident signal in VLASS at the location of the system, suggesting the source could be radio-loud.

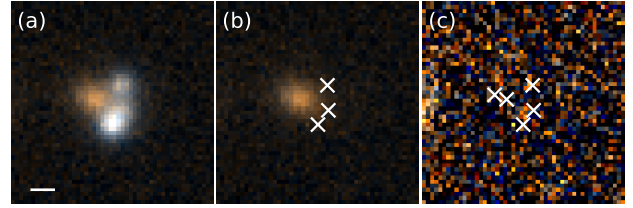


**Figure 14.** (a) CFHT  $rz$  colour image of J0833+2612 with a  $1''$  scalebar, (b) data with 3 PSFs subtracted showing the galaxy and bluer counterimage, (c) residuals after subtracted a 4 PSF + Sersic model.

## 4.1.27 J0907+6224

This double has both SDSS and BOSS spectra. It has a source redshift of  $z=1.86$  and a separation of  $2.48''$ . The BOSS spectrum shows two narrow absorption features in the C IV line. The different continua between the BOSS and SDSS spectra is likely attributed to the different fibre apertures ( $2$  and  $3''$  respectively), and contamination from the lensing galaxy. The SDSS pipeline catalogues this as two objects, with an  $i$ -band magnitude of 18.93 for the Northern component, allowing a colour selection from SQLS to select this as a potential lens. The likely reason this was not selected was due to a colour difference in  $g-r$  between the two components;  $0.54$  and  $1.01$  for the quasar and companion respectively (Oguri et al. 2006).

## 4.1.28 J0911-0948

This double lens is associated with an XMM serendipitous source with a flux of  $8.6\pm 1.3\times 10^{-14}$  erg cm $^{-2}$  s $^{-1}$  in the 0.2–12keV band (Webb et al. 2020).

## 4.1.29 J0918-0220

This double was confirmed during the 2019 WHT observations, revealing a source redshift of 0.803, and a lens redshift of 0.460. This system was also independently selected as a lens candidate by Sonnenfeld et al. (2020) and confirmed in Jaelani et al. (2021) who report consistent redshifts.

## 4.1.30 J0921+3020

This  $2.93''$ -separation double has a source redshift of  $z=3.33$ , with one bright image ( $G=18.66$  with SDSS and BOSS spectra), and one faint image ( $G=20.86$ ) blended with a galaxy. The lens redshift of this double is seen in the difference spectra between the two components, showing clear absorption lines at  $z=0.428$ . There are two galaxy clusters surrounding this lens, with spectroscopic redshifts from SDSS spectra of  $z=0.334$ ,  $z=0.427$ . Therefore, the lens belongs to the latter cluster. The system lies in the Smithsonian Hectospec Lensing Survey (SHELS) four degree field, and both objects have SHELS spectra of  $z=3.33$  quasars (Geller et al., 2014). The system has radio and X-ray counterparts in FIRST ( $4.33\pm 0.14$  mJy at 1.4GHz), SZA ( $2.9$  mJy at 5GHz,  $1.4$  mJy at 31GHz, Muchovej et al. 2010), VLASS ( $3.5\pm 0.5$  mJy at 2–4GHz, clearly resolved into two components, Gordon et al. 2021), and XMM-Newton ( $3.0\pm 0.8\times 10^{-14}$  erg cm $^{-2}$  s $^{-1}$  in the 0.2–12keV band, Webb et al. 2020).



## 4.1.31 J0936-1211

The NTT-EFOSC2 spectrum shows two clear traces, one of a  $z=2.00$  quasar with a very blue continuum, and one red trace with absorption features of a  $z=0.260$  galaxy. There are hints of broad emission features including C $\text{IV}$  and the blue continuum in this latter trace. Indeed, the two *Gaia* detections coupled with the alignment of the background quasar within  $2.1''$  of the foreground galaxy strongly suggests the presence of a counterimage. Two PSFs and a galaxy are required for clean residuals of the Pan-STARRS imaging, with the second PSF in the location of an expected counterimage, namely  $0.9''$  from the galaxy opposite the bright image. We therefore classify J0936-1211 as a lensed quasar, however, deeper imaging is needed to definitively confirm this.

## 4.1.32 J1003+0651

This double has three GDR2 detections, centred on a SDSS spectroscopic galaxy at  $z=0.225$ . A feature around  $4300\text{\AA}$  is indicative of a quasar, and subtraction of the SDSS model galaxy template reveals quasar emission lines at  $z=2.56$ . Our WHT data resolve two quasar traces at the same redshift, either side of the lensing galaxy, thus confirming this system as a lensed quasar.

## 4.1.33 J1008+0046

This system has a spectroscopic redshift of  $z=1.511$  from the 2df quasar redshift survey (Croom et al. 2004). Our follow-up WHT resolve two quasars at this redshift and HSC imaging clearly reveals a lensing galaxy.

## 4.1.34 J1037+0018

The NTT-EFOSC2 spectra show two quasars at  $z=2.462$ , in agreement with a 2dF spectrum at  $z=2.464$ . This system has HSC DR3 data, which clearly shows a lensing galaxy upon subtraction of the two PSFs.

## 4.1.35 J1041+1710

The NTT-EFOSC2 spectra resolve two quasars at  $z=2.00$ , with two broad absorption line features in both the C $\text{IV}$  and Si $\text{IV}$  lines. A lensing galaxy is seen in the PSF-subtracted Legacy Survey imaging.

## 4.1.36 J1233-3542

This double has two bright *Gaia* detections ( $G=18.54, 19.56$ ) separated by  $2.08''$ . The WHT spectrum reveals particularly narrow quasar emission lines at  $z=2.28$ . Archival DECam *giz* imaging shows clear residuals upon subtraction of two PSFs, thus we classify this system as a lens.

## 4.1.37 J1247-3253

This double has two bright components ( $G=18.27, 19.09$ ) separated by  $1.85''$ . NTT-EFOSC2 spectroscopy reveals very similarly shaped spectra of quasars at  $z=1.66$ . Shallow archival *griz* DECam imaging shows residual flux in the  $z$ -band, which we take as a detection of the lensing galaxy.

## 4.1.38 J1255+0737

WHT-ISIS long-slit spectra were taken with the slit position angle at  $5.6$  degrees East of North. The spectra reveal two quasars at  $z=2.145$ . In *Gaia* EDR3 there is a third detection associated to a galaxy  $2$  arcseconds to the East, which could be due to another image of the source blended with the galaxy, as in the case of SDSSJ1405+0959 (Rusu et al. 2014). High-resolution imaging is needed to see if this is an interesting case of a lens with two lens planes and three images.

## 4.1.39 J1303+1816

A  $G=12$  star lies  $15''$  from this lens, offering a good opportunity for natural guide star adaptive optics observations of the system. The galaxy lies in a group, with one nearby galaxy having an SDSS spectroscopic redshift of  $z=0.410$ , and a further one with  $z=0.473$ . Clear signs of a  $z=0.46$  lensing galaxy are seen in the spectrum of the fainter image.

## 4.1.40 J1307+0642

This system was first selected as a lens candidate by Lemon et al. (2019), however, the spectra were too shallow to detect quasar emission lines. The new 1200s WHT-ISIS exposure shows clearly two traces of a  $z=2.03$  quasar, with the fainter image blended with a  $z=0.23$  galaxy. A SDSS spectrum confirms our redshift of the lensing galaxy. Archival Chandra data – originally from observations of 3C281, which is situated less than  $3$  arcminutes from this system – resolve two X-ray point sources coincident with two optically blue point sources either side of a bright galaxy. The fluxes of the two components are  $3.7\pm 1.9 \times 10^{-14}$  and  $0.9\pm 0.4 \times 10^{-14}$  erg  $\text{cm}^{-2}$   $\text{s}^{-1}$  in the broad  $0.5\text{--}7\text{keV}$  band.

## 4.1.41 J1326+3020

The WHT spectrum reveals two traces, one of a quasar at  $z=1.852$ , and another of a galaxy at  $z=0.339$ . The Legacy Survey imaging shows a blue point source in the model-subtracted residual image, suggesting this as a faint counterimage. Indeed there are hints of the Ly $\alpha$  line in the blue arm raw pixels of the WHT-ISIS data, thus we classify this as a lens. The lens is a member of a cluster, whose members were targeted for spectroscopy by Holden et al. (1999). They obtained a spectrum for the lensing galaxy of this system, reporting a broad emission line around  $5437\text{\AA}$ , which they attributed to MgII, giving a tentative redshift of  $z=0.94$ , however our spectra confirm this is in fact the CIII] line in agreement with an archival eBOSS spectrum centred on the galaxy.

## 4.1.42 J1526-1400

This double has the lowest redshift source yet discovered for lensed quasars,  $z=0.648$ , and a particularly bright, low-redshift lensing galaxy at  $z=0.096$ . Similar to J1003+0651, the lensing galaxy is detected by *Gaia*. Given the brightness of this lens ( $i=16.02$ ), and that of J0416+7428, we can consider how many bright lensing galaxies are expected based on the OM10 mocks. With the two doubles presented here, and Q2237+030 (Huchra et al. 1985), we have 3 lenses with multiple *Gaia* detections, and lensing galaxies brighter than  $i=16.5$ . This seems to be consistent with the 4-7 expected across the whole sky based on OM10 but it is perhaps surprising given that our selection techniques are based mostly on source colours. Given these small-number statistics, investigating spectroscopic samples

of bright galaxies up to  $z=0.1$  is needed to reveal whether there is an overabundance of low-redshift lensing galaxies compared to the mocks.

#### 4.1.43 J1550+0221

This double has a BOSS spectrum, and was selected as a lens candidate independently by Spiniello et al. (2018) using pixel analysis of Kilo-Degree Survey imaging.

#### 4.1.44 J1945-2857

This double has two *Gaia* detections separated by  $2.69''$ , with clearly resolved spectra of a  $z=2.56$  quasar in the NTT-EFOSC2 data. The 2D PSF-subtracted spectrum shows residuals around the  $\text{Ly}\alpha$  line below both images, suggesting either a PSF not well-fit by the Moffat used (however no such residuals are seen anywhere else in the subtraction), or  $\text{Ly}\alpha$  is spatially resolved, suggesting a bright lensed host galaxy or even secondary quasar source. High-resolution imaging is needed for this system.

#### 4.1.45 J2017+6204

Two NOT-ALFOSC 900s spectra were taken at position angles of  $124.2$  and  $50.7$  degrees East of North, however both showed a blended trace of a  $z=1.72$  BAL quasar. Adaptive optics imaging with OSIRIS on Keck 2 resolves the four images and lensing galaxy, and is shown in Figure 2. The system was also independently observed by Stern et al. (2021) who obtained unresolved spectroscopy, corroborating our reported redshift.

#### 4.1.46 J2110-3755

The NTT-EFOSC2 spectrum is low signal-to-noise, however, two traces are clearly visible, with at least one associated to a  $z=1.50$  quasar. Given the extended residuals in the Legacy Survey  $r$ -band image when fit with just two PSFs and the extended  $\text{MgII}$  emission across both traces, we classify this system as a lens.

#### 4.1.47 J2205+1019

While the extracted 1D spectra only show quasar emission lines in one trace, the residual 2D spectrum clearly shows Lyman- $\alpha$  flux opposite the confirmed quasar, thus confirming the presence of a counterimage. The lens is particularly low redshift at  $z=0.108$ .

#### 4.1.48 J2205-3727

This quad was selected as a *Gaia* double around a red WISE detection and visually inspected using archival DECam data, with subsequent spectroscopic confirmation with NTT-EFOSC2. The slit was positioned at  $86.4$  degrees East of North to pass through the brightest image of the cusp, and the far counterimage. *Gaia* EDR3 only catalogues one image, compared to two in GDR2.

#### 4.1.49 J2213-5926

We identify a likely lens redshift of  $z=0.545$ , however deeper spectra are required to confirm this.

#### 4.1.50 J2316+0610

This system was originally selected by Lemon et al. (2019) who suggested a possible source redshift of  $z=1.96$ , however their spectra were too noisy to conclusively confirm the system as a lens. Our deeper NOT data clearly resolve two quasars at  $z=1.955$ , thus confirming this system as a lens. The source is a BAL quasar with multiple components, confirmed by a recent eBOSS spectrum. We measure a lens redshift of  $z=0.378$ , consistent with the redshift of a nearby galaxy with a BOSS spectrum.

## 4.2 Likely Lensed Quasars

These systems are all classified as likely lensed quasars. Most are lacking the detection of a lensing galaxy, but have particularly similar resolved spectra, and thus should be prioritised for follow-up high-resolution imaging. For some systems the spectra are too noisy to confirm the presence of a counterimage, however the imaging suggest such a counterimage to be present, and thus require deeper spectroscopy.

#### 4.2.1 J0138+4841

This particularly bright, small separation pair ( $G=16.42, 17.45$ , and  $\Delta\theta=0.69''$ ) shows a clear broad emission line at  $6078\text{\AA}$ . The 2D spectrum modelling extracts very similar spectra for the two components with a flux ratio smoothly increasing from 1.8 at  $4000\text{\AA}$  to 2.4 at  $9000\text{\AA}$ , the latter of which is in good agreement with the *Gaia* flux ratio (2.6). The brighter component shows narrow absorption at the wavelength of  $\text{CIII}]$ . Modelling the Pan-STARRS data reveals extended flux, which can be reasonably well-fit around the 2PSFs when including a Sersic profile which falls between the two sources, suggesting it is a lensing galaxy. Given the small-separation and the only available imaging data being low-resolution, we suggest obtaining additional high-resolution imaging before designating this system as a sure lens. This system is also associated to both a ROSAT X-ray source and a radio source in VLASS ( $1.65\pm 0.35\text{mJy}$  at  $2-4\text{GHz}$ ).

#### 4.2.2 J0149-6532

The imaging for this system clearly shows two blue PSFs either side of a luminous red galaxy (LRG). The spectrum of the brighter blue source is low signal-to-noise and shows only hints of a quasar spectrum at  $z=0.944$ .

#### 4.2.3 J0221+0555

The resolved ALFOSC-NOT spectra show very similar  $z=1.52$  quasar profiles, with both components having strong absorption bluewards of the  $\text{CIII}]$  line and similar narrow  $\text{CIV}$  profiles. Since no residual lens galaxy is seen in the imaging.

#### 4.2.4 J0326-3122

This system was already reported by Schechter et al. (2017) as a lensless twin at  $z=1.34$ , with narrow absorption at  $z=0.504$ . We obtained EFOSC-NTT spectra of the system across a larger wavelength range, revealing the  $\text{MgII}$  emission line of the components. Our results qualitatively agree with those of Schechter et al. (2017). A galaxy is seen about  $1''$  North of the system in the PSF subtracted

Legacy Survey images, possibly responsible for the  $z=0.504$  absorption in image A.

#### 4.2.5 J0326-4950

The Legacy Survey imaging residuals for this system show an extended galaxy coincident with one of the *Gaia* detections, as well as possible faint blue point source. The spectra are low signal-to-noise but the galaxy is determined to be at  $z=0.229$  through emission lines. The other blue point source is likely a  $z=1.72$  quasar, however this is not definite. The system could still be acting as a lens, so deeper imaging and spectroscopy are required. The system is associated with a ROSAT X-ray source.

#### 4.2.6 J0332-6608

This system consists of two bright point sources ( $G=18.30, 19.46$ ) separated by  $0.94''$ . NTT-EFOSC2 spectra reveal similar emission lines of a  $z=1.97$  quasar, with a constant flux ratio of  $\sim 2.5$  except for a differing depth of an absorption line at  $4860\text{\AA}$ . Only Legacy Survey  $g$  and  $r$ -band data is available, and no obvious lens is seen upon subtracting the two PSFs.

#### 4.2.7 J0346+2154

This  $0.99''$ -separation system was targeted for NOT-ALFOSC spectroscopy, which confirmed the presence of two quasar spectra at  $z = 2.365$ . The system was also independently selected by Krone-Martins et al. (2019) as a lens candidate. They obtained resolved spectroscopy and suggest this is most likely a lensed quasar given the similar narrow absorption associated with the blue wing of C $\nu$ . We also note this absorption line, and striking similarity between the two spectra, with the only slight differences being in the height of the C $\nu$  and C $\text{III}]$  lines, which is likely explained by microlensing. We model CFHT MegaCam stacked  $i$ -band data as 2 PSFs, however the PSF model is not good enough to clearly tell if there are residuals from a possible lensing galaxy.

#### 4.2.8 J0916-2848

While the continua of the two components are quite different, the emission lines have similar profiles. If the system is a lens, the different continua can be explained by the presence of a lensing galaxy and/or microlensing, as has been seen in other systems, for example GRALJ2343+0435 (Krone-Martins et al. 2019). A prominent absorption line is seen in only the fainter component at  $4463\text{\AA}$ . No significant residuals are detected upon PSF subtraction in the Pan-STARRS data.

#### 4.2.9 J1008-2911

The EFOSC2 extracted spectra show two quasars at  $z=2.49$  with very similar line profiles and continua, suggesting this is a likely lens. However, no residuals are seen in either the Pan-STARRS PSF-subtracted image or archival DECam  $gri$  imaging.

#### 4.2.10 J1019-1322

The NTT-EFOSC2 spectra reveal two quasars at  $z=2.325$  with similar continua and line profiles, however no galaxy is seen in the Pan-STARRS imaging residuals.

#### 4.2.11 J1033-8249

NTT-EFOSC2 spectra of this  $2.33''$ -separation double reveals two quasars with similar profiles at  $z=1.69$ . The spectra appear to have a red continuum, however slit losses due to atmospheric refraction and high airmass observations cannot be entirely ruled out despite our correction model. Shallow archival NOAO data exist for this system, however no obvious lens light is seen upon subtracting two point sources.

#### 4.2.12 J1036-8544

NTT-EFOSC2 spectra of this  $1.22''$ -separation double reveals two quasars with similar continua and MgII lines at  $z=1.09$ . Shallow archival NOAO data clearly show the two point sources detected by *Gaia*. Subtracting two PSFs from the available  $r$  and  $i$  band data reveal some faint residuals around the system, likely due to a lensing galaxy. We currently classify this system as a likely lens, requiring deeper imaging data.

#### 4.2.13 J1103-1005

This  $0.72''$ -separation system has two bright *Gaia* detections ( $G=17.79, 18.01$ ), and NTT-EFOSC2 long-slit spectroscopy shows spatially resolved traces of a  $z=1.29$  quasar. The emission line profiles are very similar, with a difference in the slope of the continua in the blue. The flux ratio varies smoothly from 1.9 to 1 between  $4000$  and  $8000\text{\AA}$  respectively. This is a very likely lens with the spectrum differences attributed to reddening by a lensing galaxy and/or microlensing. There are hints of an extended source in the Pan-STARRS  $i$ -band PSF-subtracted image, however we suggest higher-resolution imaging is required to confirm this system as a lens.

#### 4.2.14 J1322+7852

This system was selected as a *Gaia* double with a red WISE source. In Pan-STARRS and Legacy Survey imaging, there is clearly one blue point source next to a galaxy, and WHT-ISIS spectroscopy shows two traces. The galaxy trace shows both an old stellar population with an obvious  $4000\text{\AA}$  break and common LRG absorption lines, but also narrow star formation emission lines. The trace of the blue PSF is almost featureless and low signal-to-noise, however binning the spectrum reveals broad emission lines of a  $z=2.165$  quasar. No spectral features of this quasar appear in the trace of the galaxy as a possible counterimage, however such features would be expected to be too faint if a counterimage exists. The Legacy Survey residuals show a very faint possible counterimage. Deeper spectra and/or imaging are needed to confirm this as a counterimage.

#### 4.2.15 J1350+3155

An archival SDSS spectrum of this system shows a galaxy at  $z=0.211$ . Our spectrum corroborates this redshift for the galaxy, and also shows that the nearby blue PSF is a quasar at  $z=1.895$ , however no quasar emission lines are seen in the combined  $1500\text{\AA}$  extraction of the galaxy. We expect that the quasar is strongly lensed given the small separation between the *Gaia* detections of  $1.44''$ , and the high velocity dispersion of the galaxy ( $238\text{ km s}^{-1}$ ). We estimate the Einstein radius of this lens given this dispersion, the source and lens redshifts, and assuming a singular isothermal sphere mass profile, obtaining  $\theta_E \approx 1.35''$ . Generally, images of such a

profile are separated by twice the Einstein radius, i.e.  $2.7''$ . The likeliest solution is that the counterimage is highly demagnified, either through microlensing, or extinction/reddening by the lensing galaxy, or some combination of both. High-resolution imaging for this system should be prioritised to search for a counterimage.

#### 4.2.16 J2244-0550

NTT-EFOSC2 spectra show both components to be quasars at  $z=2.84$  with almost identical profiles. However, no lens residuals are seen in the Pan-STARRS or Legacy Survey PSF-subtracted images.

#### 4.2.17 J2255+8009

The NOT-ALFOSC spectroscopy resolves two quasars with very similar spectra and a pronounced drop in flux below  $4650\text{\AA}$ , either due to intrinsic quasar emission or line-of-sight absorption. Two deep absorption features are seen at  $4607\text{\AA}$  and  $4650\text{\AA}$  consistent with absorption from Ca H and K at  $z=0.172$ , however, no other clear absorption features at this redshift are seen in the spectra. The emission lines are likely associated with a  $z\approx 2.8$  quasar, implying that Ly $\alpha$  is strongly absorbed (and perhaps these two absorption lines are due to proximate damped Ly $\alpha$  systems). The Pan-STARRS data are well fit by two PSFs.

### 4.3 Unclassified Quasar Pairs

The following systems have resolved spectroscopy showing two quasar components at consistent redshifts, however they lack the spectral signal-to-noise and/or lens galaxy detection to be classified as a (likely) lensed quasar.

#### 4.3.1 J0124-6334

The Legacy Survey image of this system shows two point sources of different colours, and subtracting 2 PSFs shows clear extended residuals between the PSFs. When including a Sersic profile, the data are well fit, with the position of the Sersic falling between the two PSFs closer to the fainter image, consistent with that expected of a lensing galaxy in a typical double configuration. The best-fit Sersic index is  $\sim 1$ , typical of spiral galaxies. The spectra are low signal-to-noise and overlap due to poor seeing and small separation, however binning the spectra shows large differences between them, with different continua, broad emission line profiles, and relative intensities (e.g. OIII is present in the fainter image). Thus the lensing scenario is unlikely, but not necessarily ruled out due to differential extrinsic effects like strong absorption and/or microlensing. If these are indeed distinct quasars, the projected separation of  $0.87''$  is  $6.52$  kpc at  $z=1.30$ .

#### 4.3.2 J0125-1012

The two components of this system have similar spectra of a  $z=1.22$  quasar, but no definite lensing galaxy is detected in the available imaging.

#### 4.3.3 J0127-1441

The NTT-EFOSC2 spectra reveal the two components to be similar quasars at  $z=1.754$ , however there is only a faint red source ( $i < 22$ ) South of the system seen in the PSF subtracted image. Given the wider separation of this system,  $3.00''$ , and assuming it is a lens, we can estimate the faintest possible lensing galaxy brightness. We use the Oguri & Marshall (2010) catalogue and simply search this catalogue for mock lenses with similar image separations (within  $0.5''$ ) and source redshifts (within 0.25), and consider the lens magnitudes and redshifts of the remaining systems as the possible range of lensing galaxy parameters for J0127-1441. 279 systems are recovered, with median and  $1\sigma$  uncertainties in redshift and  $i$ -band magnitude of  $0.44 \pm 0.18$  and  $19.08 \pm 1.01$  respectively. The lens properties of the system with the faintest lensing galaxy are  $z=0.974$  and  $i=20.6$ . It is thus unlikely that the faint source is a lensing galaxy.

#### 4.3.4 J0130+0725

The spectra show two quasars at  $z=1.54$  with different emission line profiles, as there is prominent absorption in the CIV and MgII lines of the fainter quasar. This is likely explained by the system being a projected pair with some small velocity separation, and line-of-sight absorption by the host galaxy of the closer (brighter) quasar. A higher resolution archival eBOSS spectrum indeed resolves both the MgII  $2800\text{\AA}$  and CIV  $1549\text{\AA}$  absorption doublets (Blanton et al. 2017). No residuals are seen in the PSF-subtracted images. Intrinsic absorption along different sightlines to the same source quasar cannot necessarily be ruled out.

#### 4.3.5 J0133+0816

The spectra reveal two quasars at  $z=1.27$ , with small differences in the widths of the CIII] and MgII emission lines. Modelling deep CFHT  $r_{iz}$  Megacam stacked data as two PSFs reveal no obvious lensing galaxy.

#### 4.3.6 J0146-6510

The two components have very similar NTT-EFOSC2 spectra of a quasar at  $z=1.255$ , however no lens is seen in the Legacy Survey  $z$ -band residuals after fitting 2 PSFs. The system is associated with a radio source in GLEAM ( $0.555 \pm 0.011$  Jy at  $170\text{--}231\text{MHz}$ , Hurley-Walker et al. 2017), and SUMSS ( $214 \pm 9$  mJy at  $843\text{MHz}$ , Mauch et al. 2003), and an X-ray source (Slew Survey XMMSL2 Catalogue,  $2.3 \pm 1.1 \times 10^{-15}$  Wm $^2$ , Saxton et al. 2008).

#### 4.3.7 J0311+0550

The NOT spectrum of this system reveals the two components to have similar spectra of a  $z=0.777$  quasar, however modelling the Pan-STARRS data as two point sources does not show any significant residuals.

#### 4.3.8 J0527-2431

The NTT-EFOSC2 spectrum shows two resolved traces with emission lines of a  $z=1.437$  quasar, but with differences in the line profiles and relative intensities. Deeper spectra and/or imaging are required to definitively classify the two components as distinct quasars, separated by  $1.46''$ , i.e.  $12.5$  kpc.

#### 4.3.9 J0642+5337

The NOT-ALFOSC resolved spectrum shows two quasars at  $z=1.86$ , with several narrow absorption lines in the brighter component. This is likely a distinct quasar pair due to the lack of lens in the PSF-subtracted Legacy Survey image, the different C<sub>IV</sub> profile, and the sky separation of  $3.17''$ .

#### 4.3.10 J0723+4739

This pair shows no residuals in PSF-subtracted Legacy Survey imaging, and the peaks of the MgII profiles are offset in velocity. Given possible extrinsic absorption in a lensing configuration causing this difference, we categorise the system as an unclassified quasar pair, but likely a binary quasar. If the components are indeed distinct quasars, their projected separation would be  $10.9$  kpc ( $1.58''$ ). Deeper spectra and imaging are required. This system was targeted by [Lemon et al. \(2018\)](#) but their results were inconclusive due to low signal-to-noise.

#### 4.3.11 J0728+2607

The NOT-ALFOSC spectrum shows two quasars at  $z=1.025$ , with large differences in their emission line profiles and continua, thus making it a likely physical quasar pair. Their projected separation is  $17.6$  kpc at  $z=1.025$  ( $2.15''$ ).

#### 4.3.12 J0816+2339

Despite the WHT spectrum being low signal-to-noise, the two components are clearly quasars at  $z=1.22$ . This is likely a distinct quasar pair given the slight differences in the MgII profile.

#### 4.3.13 J0833-0721

The NTT-EFOSC2 spectrum shows two similar traces of a  $z=0.828$  quasar, however there is a small offset in the OIII-4960 and 5008Å lines, which appears to be real in the 2D spectrum. This would immediately rule out the lensing hypothesis, however the spectra are particularly similar, and small wavelength variations in the spatial direction could explain the apparent offset. No lens is seen in the Pan-STARRS imaging residuals. Further spectra are required to confirm a velocity difference in the OIII lines. If the quasars are indeed distinct, the projected separation would be  $9.39$  kpc.

#### 4.3.14 J0909-0749

The NTT-EFOSC2 spectra resolve this  $0.81''$ -separated pair, showing clear  $z=1.075$  quasar emission lines in each component, however the continua are significantly different. Modelling the Pan-STARRS data as 2 point sources shows no significant residuals in the redder bands. The system is associated with a VLASS detection with a flux of  $2.6 \pm 0.3$  mJy.

#### 4.3.15 J0941-2443

The NTT-EFOSC2 spectrum shows two traces, each with an emission line around  $5400\text{\AA}$ . This is most likely MgII, as then other common emission lines would fall outside the wavelength range of our spectrum. CIII] would then lie at the very bluest end of our spectrum, and indeed an increase in flux may hint at the red wing

of this emission line. The MgII profiles are different, and there is no apparent lensing galaxy in the PSF-subtracted Legacy Survey or Pan-STARRS imaging. This is likely a distinct quasar pair, with a projected separation of  $15.8$  kpc ( $2.25''$ ).

#### 4.3.16 J1045+3433

WHT-ISIS spectroscopy reveals two components with similar spectra of a  $z=1.205$  quasar. No lens seen in Legacy Survey residuals but emission lines and continua are similar enough to warrant deeper follow-up imaging.

#### 4.3.17 J1102+3421

The WHT-ISIS spectrum reveals two quasars at  $z=1.405$ , however strong absorption is seen in the C<sub>IV</sub> line of only the fainter component. Coupled with no lens residuals in the PSF-subtracted Pan-STARRS residuals, this system is likely a physical quasar pair, with the fainter component at slightly higher redshift than the bright component, however differential line-of-sight absorption in a lensing scenario cannot necessarily be ruled out.

#### 4.3.18 J1202+0703

This  $1.21''$ -separated pair shows two spatially resolved traces of a  $z=2.187$  quasar in the NTT-EFOSC2 spectrum, with each trace having similar continua and profiles, except for absorption in the C<sub>IV</sub> line of the fainter trace. No lens is seen in the residuals.

#### 4.3.19 J1428+0500

This system was previously followed up by [Lemon et al. \(2019\)](#) who concluded the two components had spectra of quasars at  $z=1.38$ . Our new WHT-ISIS spectra now reveal the C<sub>IV</sub> profile and place both quasars at  $z=1.375$ , with differing MgII profiles due to absorption in the fainter component. The Legacy Survey data are well fit by two PSFs. If the quasars are distinct, the projected separation of  $2.23''$  translates to  $17.0$  kpc at  $z=1.375$ .

#### 4.3.20 J1449-2025

EFOSC2-NTT spectroscopy shows that both components of this  $1.17''$ -separation pair are quasars at  $z=0.594$  with similar spectra. A two PSF fit to the Pan-STARRS imaging shows significant residuals around the system, as expected if the system is either a lens (residuals due to a lensing galaxy) or simply a distinct quasar pair (residuals due to the quasar hosts given the low redshift). Adding a single Sersic fits these residuals and this component falls between the two PSFs. If this system is a distinct pair, the projected separation would be  $7.9$  kpc.

#### 4.3.21 J1821+6005

The NOT-ALFOSC spectrum shows two traces of quasar at  $z=2.052$  with similar continua, but a slight difference in the shape of the C<sub>IV</sub> line. [Lemon et al. \(2018\)](#) also presented WHT-ISIS follow-up of this system, concluding the system to be a distinct quasar pair. No lens is seen in the PSF-subtracted Pan-STARRS, Legacy Survey, or CFHT *r*-band imaging.

4.3.22 *J1832+5349*

The two components of this system are separated by  $3.03''$ , and NOT-ALFOSC spectra reveal two quasars at  $z=1.16$ , with similar MgII emission line profiles and continua. However, no lensing galaxy is seen in the Legacy Survey residuals after PSF subtraction. In Pan-STARRS there is a hint of residual flux between the two quasars in the *Y*-band. Given the separation and relatively low redshift, we expect this is a distinct quasar pair.

4.3.23 *J2008+0438*

This system lies in a high stellar density environment, at a galactic latitude of  $-14^\circ$ . One trace of the NOT-ALFOSC spectra is clearly a quasar at  $z=1.70$ , however the other does not have similarly obvious broad emission lines. The latter trace has a broad emission line at the same wavelength as the MgII line of the first trace, however the telluric absorption band obscures the red wing. There is a hint of a line at the same wavelength as CIII] of the first trace suggesting this source is also a quasar at  $z=1.70$ , but no CIV emission is seen.

4.3.24 *J2057+0217*

The NOT-ALFOSC spectra show two components with similar continua but different emission line profiles suggesting a distinct quasar pair. If true, the sky separation of  $1.16''$  would correspond to a physical projected separation of 8.9 kpc at  $z=1.52$ . The WHT-ISIS observations of this system by [Lemon et al. \(2018\)](#) do not reveal a CIV emission line as we see in these newer spectra, which is likely due to unaccounted slit losses.

4.3.25 *J2341-1557*

NTT-EFOSC2 spectra of this small-separation system ( $1.02''$ ) reveal two quasars at  $z=1.535$  with different continua and relative emission line strengths. It is likely a distinct quasar pair – and thus would have a projected separation of 8.8 kpc.

## 4.4 Physical Quasar Pairs

4.4.1 *J0041-5350*

Resolved spectra show that each component of this system is a quasar at  $z=0.55$ , however the lensing scenario is ruled out since the OIII profiles are very different. The extended asymmetric flux seen in the ground-based imaging is likely a sign of an ongoing merger between the two quasar host galaxies. The sky separation of  $1.06''$  translates to 6.2 kpc, making it one of the smallest separation confirmed quasar binaries above  $z=0.5$  ([Chen et al. 2022](#)).

4.4.2 *J0315-3522*

Legacy Survey imaging shows two point sources and a galaxy offset to one side of the fainter component. NTT-EFOSC2 spectra reveal two quasars at  $z=0.457$ , with residuals around OIII-5008Å suggesting spatially resolved emission. Given the difference between the spectra for both the continua and emission line profiles, and lack of lensing galaxy candidate in the imaging, we designate this system as a distinct quasar pair. The separation is  $1.30''$  at  $z=0.457$  – a projected separation of 6.9 kpc.

4.4.3 *J1116-2122*

Given the  $3.29''$  separation and relatively low redshift sources ( $z=0.709$ ), we categorise this as a distinct quasar pair. The projected separation is 23.9 kpc.

4.4.4 *J2121+1713*

The spectra reveal two quasars at  $z=0.63$ , however, the emission lines and continua are markedly different. Given also the low redshift, large separation of  $2.89''$ , and lack of lensing galaxy in the residuals, we classify this system as a distinct quasar pair. The projected physical separation is 17.9 kpc.

4.4.5 *J2132+3635*

The NOT-ALFOSC spectrum shows two quasars at  $z=1.215$  with slight differences in the MgII profile. Follow-up OSIRIS imaging reveals no lensing galaxy (Figure 2), thus we designate this as a distinct quasar pair. The sky separation of  $1.33''$  translates to a physical projected separation of 9.9 kpc.

4.4.6 *J2256+2223*

Despite similar profiles of a  $z=0.75$  quasar, the OIII narrow emission lines are slightly offset in wavelength. This cannot be a calibration drift in the spatial direction since the sky emission lines stay within the same pixel centroid across the width of the system and over several tens of arcseconds. Therefore, this is a distinct quasar pair with sky separation of  $1.63''$ , translating to 10.7 kpc in projected separation at  $z=0.75$ .

4.4.7 *J2322+0916*

ALFOSC-NOT spectroscopy shows that both components of this pair are quasars at  $z=1.20$ , in agreement with the SDSS spectrum of the fainter component. The emission line shapes and continua are different, and no residuals are seen in the PSF-subtracted Legacy Survey imaging. Therefore, we classify this system as a distinct quasar pair, with projected separation of 37.9 kpc ( $4.51''$ ).

4.4.8 *J2355-4553*

The NTT-EFOSC2 spectrum reveals two quasars at  $z=2.85$ , however one has strong broad absorption lines. We suggest this must imply that the two quasars are distinct, and thus have a projected separation of 16.7 kpc given their  $2.20''$  sky separation.

## 4.5 Projected Quasar Pairs

4.5.1 *J0027+0438*

The spectra show a bright quasar at  $z=1.972$ , and an AGN (broad H $\alpha$  emission) with extended host galaxy at  $z=0.1935$ . The projected separation of the system is  $1.92''$ . While no signs of a counterimage are seen in the imaging, the lensing scenario is still plausible as the quasar host galaxy requires only a modest Einstein radius,  $\sim 1''$ , and would explain the particularly large apparent brightness of the quasar through an associated magnification. High resolution imaging or deeper spectroscopy will be required to rule out the lensing hypothesis fully.

#### 4.5.2 J1820+3747

This projected quasar pair system is associated with an X-ray source in ROSAT. The quasar redshifts are 0.614 and 0.754, and Legacy Survey imaging and photometric redshifts suggests the system is coincident with a cluster at the background quasar source redshift.

#### 4.5.3 J2302-4154

One trace shows CIII] and MgII emission lines of a  $z=1.22$  quasar, while the other only shows one emission line at  $5540\text{\AA}$ , and no other clear emission lines. This is most likely MgII, since at this redshift no other common quasar emission lines are expected to fall within the wavelength range of our spectra. This would put the second component at a lower redshift of 0.98, with the background quasar passing at 8.7 kpc in projection.

### 4.6 Other

#### 4.6.1 J0336-3244

One trace of this system is a  $z = 0.545$  quasar, however the trace of the second object is noisy, with hints of  $z=0$  absorption lines, i.e. it is possibly a star. Deeper spectra are needed to verify this.

#### 4.6.2 J0819+0457

The signal-to-noise of the fainter trace is too low to determine any robust features. It is likely that this is a distinct quasar pair or quasar-star projection, however deeper spectra are needed.

#### 4.6.3 J0938+0629

The spectrum shows resolved narrow line emission at  $z=0.363$ , however only the brighter component has broad emission lines. We therefore classify this as a quasar+galaxy pair.

#### 4.6.4 J1140+2303

The resolved spectra show a  $z=2.405$  quasar and a likely star given  $H\alpha$  and  $H\beta$  absorption at  $z=0$ . However, there are also similarities between the two spectra, in particular around the wavelength of Lyman alpha, which is unlikely to be due to extraction problems given the wide separation of  $3.63''$ . We suggest this is a quasar-star projection, however, deeper spectroscopy and/or imaging is needed to definitively conclude this.

#### 4.6.5 J1442-0857

The extracted spectra reveal galaxies at  $z=0.164$ , the redder one of which has strong narrow line emission (OII,  $H\alpha$ , NII, SII). The redder component also appears to be coincident with a bright radio detection in VLASS.

#### 4.6.6 J1752+0826

This system appears as two blue point sources either side of a galaxy, however follow-up WHT-ISIS spectra reveal likely  $z=0$  absorption lines in both traces, alongside narrow line emission at the redshift of the galaxy,  $z=0.3195$ . Such similarities to double quasar configurations are expected at high stellar densities. This system lies at a galactic latitude of  $b=15^\circ$ .

### 4.7 Lensed galaxies

As a by-product of looking for lensed quasars, lensed galaxies may be discovered semi-serendipitously since they share unique morphological similarities with lensed quasars, namely multiple blue detections around luminous red galaxies. We present four new lensed galaxies that were found in our searches, two with single *Gaia* detections and two with two blue SDSS detections around a red galaxy.

#### 4.7.1 J0343-2828

This lens was selected as a potential lensed quasar candidate through the single *Gaia* detection offset method using DR2 ( $G_{DR2} = 21.29$ ), and looked promising given the compact PSFs. However, spectroscopic follow-up with the NTT in October 2019 confirmed the source as a  $z=1.655$  galaxy, with a lens at  $z=0.385$ . The coordinates are: R.A., Dec. = (55.7978, -28.4779). *HST* imaging (*HST* Proposal 15652, P.I.:Treu) shows that indeed the images are not consistent with point sources, and further show two lensing galaxies with a fifth image between them (Schmidt et al. 2022).

#### 4.7.2 J0500-5534

This lens was selected as a potential lensed quasar through the single *Gaia* detection offset method in *Gaia* DR2 ( $G_{DR2} = 20.28$ ) and a marginally red colour of  $W1-W2=0.53$ . The coordinates are: R.A., Dec. = (75.1017, -55.5796). The DES imaging is well-fit by four point sources and a Sersic galaxy profile, with the positions forming a short-axis cusp configuration, which is indeed well-fit by an SIE+shear lens model. Follow-up spectroscopy with FIRE on the 6.5-meter Baade Magellan telescope shows clearly resolved narrow emission lines of a  $z=0.620$  galaxy. Figure 15 shows the 1D spectrum, with the following emission lines marked:  $H\alpha$ , [SIII], and HeI. In EDR3, there is an additional detection for the counterimage and is the only known lensed galaxy with two *Gaia* detections to our knowledge ( $G_{DR2} = 20.84, 20.98$ ).

#### 4.7.3 J0920+4521

This system was discovered through a search for multiple blue catalogued detections in SDSS within a few arcseconds of a red photometric galaxy. Legacy Survey imaging shows a blue arc East of a group of four galaxies all with similar colours (see Figure 15). Two of these galaxies have existing SDSS spectra, one an LRG at  $z=0.546$ , and the other with narrow emission lines at  $z=0.956$ . However, closer inspection of the latter spectrum shows also an LRG spectrum consistent with  $z=0.546$ , suggesting the emission lines are from a background source, possibly a counterimage of the observed arc. Follow-up spectroscopy with ISIS on the WHT were taken on 31 March 2017 at two position angles – along the arc, and through the brightest part of the arc and the galaxy with the spectrum with narrow emission lines. The spectra are shown in Figure 15. The arc shows clear absorption lines of a  $z=2.633$  galaxy, and the galaxy spectrum is qualitatively similar to the SDSS one, showing the narrow OII emission of a  $z=0.956$  source. One possibility is that the main lensing galaxy is indeed at  $z=0.956$  and any signs of a  $z=0.546$  LRG are due to contamination or blending with a nearby galaxy. However, this is unlikely given that the ground-based imaging shows clearly similar colours between the multiple galaxies. We suggest the most likely situation is that there are two main lensing galaxies at  $z\approx 0.55$  with two sources at  $z=0.956$  and  $z=2.633$ . While the lensing

potential may be complex, if well-constrained, the system can be a very useful tool for cosmography (e.g. [Collett & Auger 2014](#)).

#### 4.7.4 J1059+4251

This system was discovered through a search in SDSS imaging for multiple photometric quasar candidates around photometric red galaxies. Follow-up spectroscopy with ISIS on the WHT on 31 March 2017 targeting the bright arc reveals a  $z=2.793$  galaxy. Figure 15 shows the 1D spectrum and the DECaLS  $grz$  colour image of the system. *HST* imaging reveals three lensing galaxies and a complex lensing configuration. This system is examined in detail in [Citro et al. \(2021\)](#).

## 5 DISCUSSION

### 5.1 Lenses

#### 5.1.1 Sample characteristics

We can compare several features of the lenses we have discovered with those previously known in order to elucidate possible biases in our selection methods and/or those of previous discovery methods. For the following analysis, we compile a list of 224 lensed quasars from the literature, mainly from the database of [Lemon et al. \(2019\)](#), but including those from more recent publications (e.g., [Desira et al. 2022](#)). Since our goal is to find lenses with optically bright images detected by *Gaia*, we remove lenses with no *Gaia* detections, or unmeasured source redshifts. From the known sample, this eliminates 38 lenses, mainly composed of CLASS radio-loud sources, lenses with faint optical images ([More et al. 2016](#); [Chan et al. 2022](#)), particularly reddened or high-redshift quasar sources (e.g., [Fan et al. 2019](#)), and two systems which have *Gaia* detections but unmeasured or insecure source redshifts: B2108+213 from [McKean et al. \(2005\)](#) and J2218-3322 from [Chen et al. \(2022\)](#). It also removes one object from the new sample, J0310-5545, which was serendipitously discovered because of a *Gaia* detection from a nearby star. This leaves 85 lenses (8 quads, 1 triple, 76 doubles) in our new sample, and 186 (2 five-image lenses, 41 quads, 3 triples, 140 doubles) in the previously known sample. We can immediately compare the multiplicity ratio of the known sample against those of this paper: the ratio of lenses with more than two images to those with just two is 46 to 140 (1 to 3.0), and 9 to 76 (1 to 8.4) respectively. These very different ratios are likely due to the ease of finding quads (generally easily recognisable even without the presence of a bright lensing galaxy) compared to doubles coupled with the bias of following up quad candidates and reporting them in earlier papers or by others (e.g., [Schechter et al. 2017](#); [Lucey et al. 2018](#)). It cannot be taken as a bias in our selection since our selection criteria recover all optically bright quads.

In Figure 16, we show the source redshift and maximum image separation of these two samples, marking the 16th, 50th, and 84th percentiles, which highlights two marginal differences: (i) the sources of the lensed quasars from this work have a higher median redshift than the known lens sample (1.94 and 1.86 respectively), likely due to redshift constraints of previous searches relying on UV-excess for pre-selection ([Oguri et al. 2006](#)); and (ii) the image separation distribution is marginally more peaked than that of the existing sample (medians of 1.83 and 1.77, and standard deviations of 0.92 and 1.07 respectively). While not significantly different populations, these differences can be explained by the cutoff at larger separations in our original selection criteria, and also the cutoff at

lower separations from our candidates which are likely lenses but do not show lensing galaxies in the shallow existing imaging. The counterparts in the existing sample have already received the necessary deeper follow-up imaging. Including these unclassified quasar pairs as lenses would remove this difference at smaller separations, but exacerbate the redshift offset between the samples. See Section 5.1.3 for a comparison of these samples to mock catalogues, to assess the relevant completeness of known lensed quasars.

#### 5.1.2 Comparing *Gaia* DR2 to *Gaia* EDR3

We investigate the differences in detection of lensed quasar images between *Gaia* DR2 and early *Gaia* DR3 (EDR3), not only to elucidate the completeness and biases in our current and previous selections, but also as a potential probe of discovering new lenses through catalogue parameter comparison. We combine the known and new samples of lensed quasars from Section 5.1.1, resulting in 274 lenses (now including those without known source redshifts). We inspect cutouts of the lenses with the detections from both data releases overlaid and note the following:

- 241 (88%) have equal numbers of *Gaia* detections between data releases; however in 3 cases detections have been replaced: HS0810+2554 ([Reimers et al. 2002](#)), the DR2 detections coincide with one of the bright pair and the Northern image, while EDR3 replaces the Northern image with the South-Eastern image – interestingly, the first data release catalogues the same images as EDR3; PSJ0840+3550 ([Lemon et al. 2018](#)), the counterimage was catalogued in DR2 but in EDR3 it has been removed and the galaxy is catalogued; and SDSSJ1251+2935 ([Kayo et al. 2007](#)), the merging pair was catalogued in DR2, but now has just the Southern image of this pair and the Western image catalogued in EDR3.
- 25 (9%) have gained one detection. For 19 of these, the detection is associated with the lensing galaxy. For 5 (3 quads, 2 doubles), the detection is associated with another image. And for 1, PMNJ0134-0931, it did not previously have a detection in DR2.
- 7 have lost a detection. 5 (1 quad, 4 doubles) have lost an image detection, 1 double (J1003+0651) has lost a galaxy detection, and 1 quad (SDSSJ1640+1932) has lost both of its image detections and gained a detection of the lensing galaxy.

Figure 17 shows an assortment of lens systems with the DR2 and EDR3 detections overlaid. Interestingly, for H1413+117, the *Gaia* position for image C is offset from the true position, i.e. from *HST* imaging, and has shifted closer to this true position in EDR3, however, it is still inconsistent with the position given the EDR3 positional uncertainty of  $\sim 6$  milliarcseconds. Conversely, the positions of the two EDR3 detections in HE1113-0641 seem to be further from the true positions than in DR2.

To investigate further these positional offsets as a possible method for finding compact quads and other lenses, we match images between DR2 and EDR3. We record the *G*-band magnitude difference and positional offset for all lensed quasar images clearly belonging to the same component (i.e. galaxy or specific image). For one image of 2M1310-1714 there is no *G* magnitude in EDR3, so this single image is omitted from our investigation. The distribution of these offsets in position and photometry are shown in Figure 18. The largest positional offsets are those of images in small separation quads, namely H1413+117, HE1113-0641, WFI2026-4536, and J2218-3322 (see Figure 17). In the absence of the raw *Gaia* data, these offsets suggest a promising avenue for discovering more compact quads through large astrometric offsets between *Gaia* data releases. However, to properly assess the efficacy of such a method



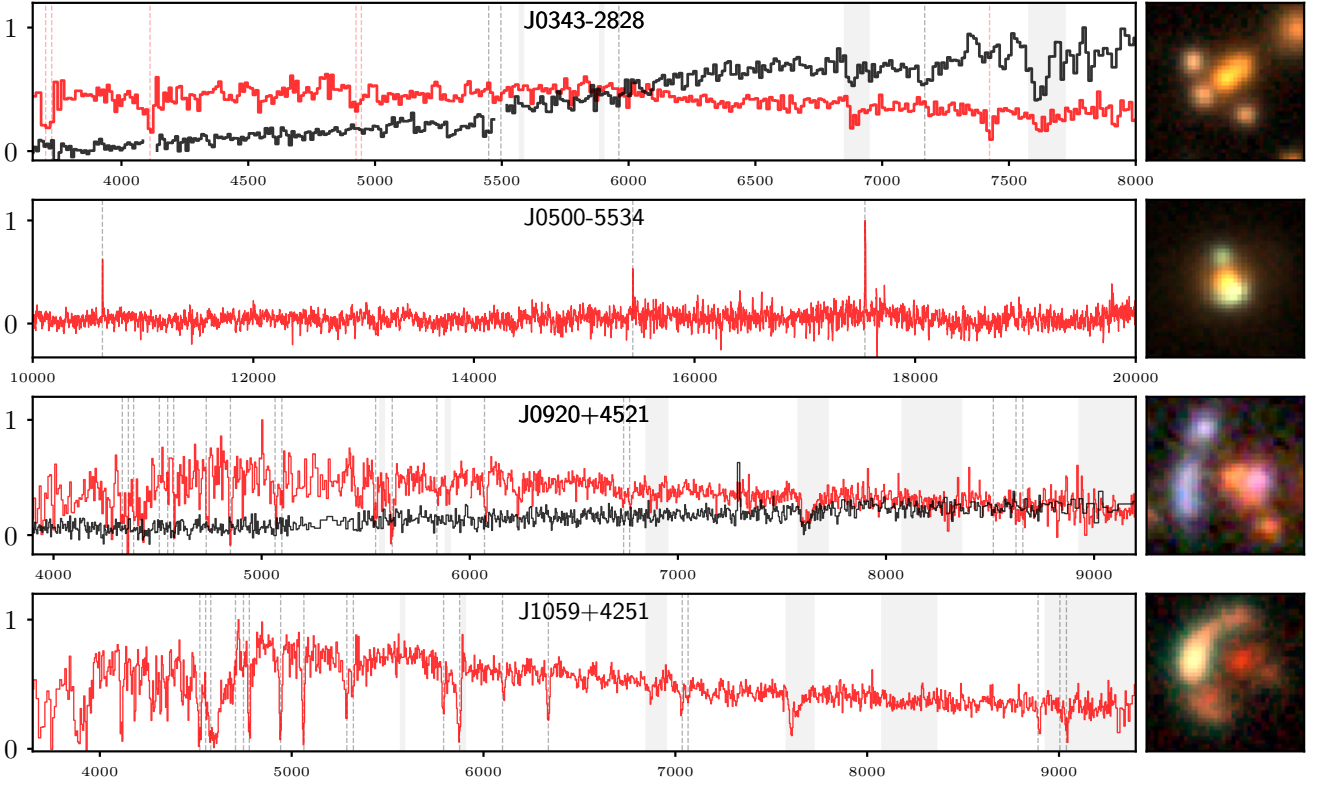


**Figure 15.** Spectra and *grz* images of serendipitously discovered lensed galaxies. Fluxes of the spectra are normalised to have a peak value of 1, and the x-axis is wavelength in Angstroms. Cutouts are from DECaLS and are 10 arcseconds on the side.

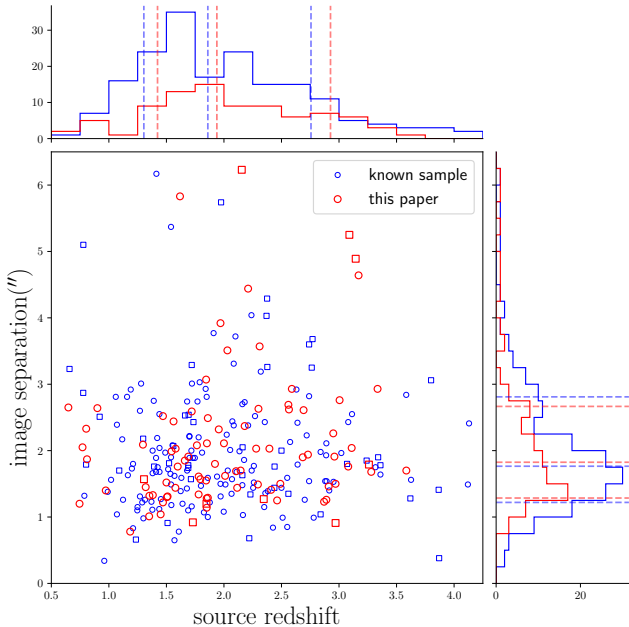


**Figure 16.** Image separation against source redshift for previously known lensed quasars (blue) and those presented in this work (red). Circles are doubles, squares are lenses with three or more images. Only those lenses falling within the image separation and source redshift limits of the plot are included in the histograms. Lines are overlaid for the 16th, 50th, and 84th percentiles of each distribution.

would require understanding the same metric distribution in common contaminants, which is beyond the scope of this paper.

There are also several systems with large photometric differences between data releases. These are all systems with bright, low-redshift, lensing galaxies. In the case of the lensing galaxy of J1003+0651, a large increase in flux (positive  $G_{DR2} - G_{DR3}$ ) is seen, and can be attributed to the counterimage being removed in the most recent data release (see Figure 17). Conversely, several galaxies have a large reduction in flux (e.g., J1526-1400 and J2205+1019), despite having the same detections in both releases. This is likely explained by a combination of deblending problems with a nearby counterimage and the known increase in variability for elongated galaxies due to average scanning direction differences (Riello et al. 2021).

### 5.1.3 Comparison to mock catalogues

We can also compare the current sample of lenses to those expected from a mock catalogue to understand the limitations of our selection. For this we use an updated version of the mock catalogue from Oguri & Marshall (2010). The updates include adopting a galaxy velocity function for all types of galaxies from Bernardi et al. (2010) combined with the redshift evolution predicted by the Illustris cosmological hydrodynamical simulation (Torrey et al. 2015) as described in detail in Oguri (2018), adopting cosmological parameters from the latest Planck satellite mission result (Planck Collaboration et al. 2020), and adopting an improved redshift-dependent model of the external shear.

We decide to compare only systems with multiple *Gaia* detections, since this is where we expect the current selection to be

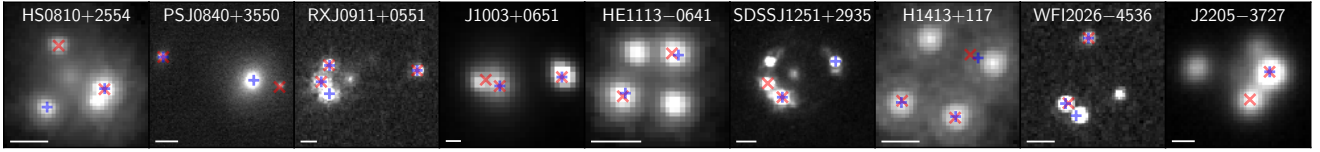


**Figure 17.** Overlay of DR2 and EDR3 catalogue detections on the best available imaging data for various interesting cases. Blue plus symbols are EDR3, while red crosses are DR2. The white scalebar represents 0.5 arcseconds. The filter has been chosen to match the peak of the *Gaia* G bandpass when possible.

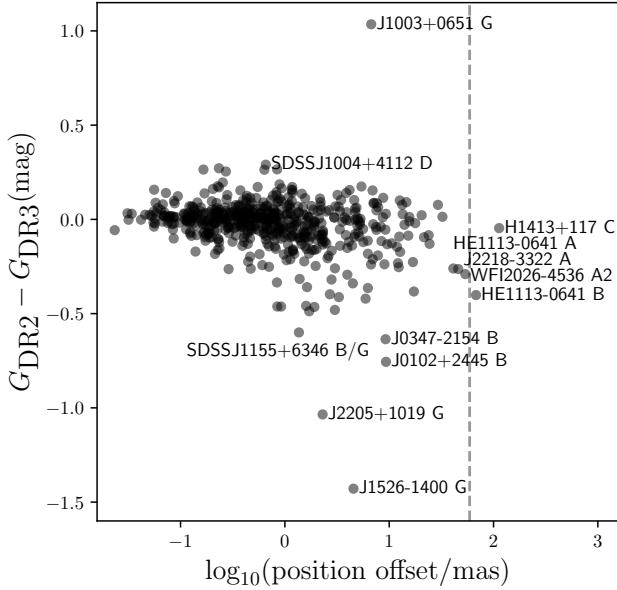


**Figure 18.** *G*-band magnitude difference against positional offset between DR2 and EDR3 for all *Gaia* detections in lensed quasars. Several outliers have been labelled and are discussed further in the text. The pixel scale of the *Gaia* detectors in the scanning direction (59 mas) is plotted as a dashed vertical line.

most complete; systems with single *Gaia* detections can have much fainter images that prevent spectroscopic confirmation. To compare the mock catalogue to the true sky, we limit the area of sky to the typical areas searched for lenses, namely those not too highly contaminated by stars. We define this as any sky area with local *Gaia* detection densities lower than 20,000 detections per square degree (as measured by the number of detections within a 100 arcsecond radius) and within the Pan-STARRS footprint, i.e. declinations above  $-30$  degrees. This leaves 53.9% of the full-sky. We also include limits on image separation of 1 to 4 arcseconds, and source redshifts below 4. These criteria keep 121 known lensed quasars. To provide mock quasars in the catalogue with *Gaia* magnitudes, we follow [Lemon et al. \(2019\)](#) by using SDSS quasars with both *Gaia* detections and measured *i*-band magnitudes, and draw a *G-i* colour for each mock source from the known quasars within 0.025 in redshift. The number of mocks that pass, normalised to the sky area used for the real lens sample, is  $\sim 214$ . The image separation and source redshift distributions are shown in Figure 19.

The predicted numbers are in good agreement with the known lenses for larger image separations and redshifts below 1.5. This is naturally explained by prioritising lens candidates with clear signs of a possible lensing galaxy, which is favoured by lower redshift sources and larger image separations.

The mock lens catalogue of [Yue et al. \(2022\)](#) underpredicts

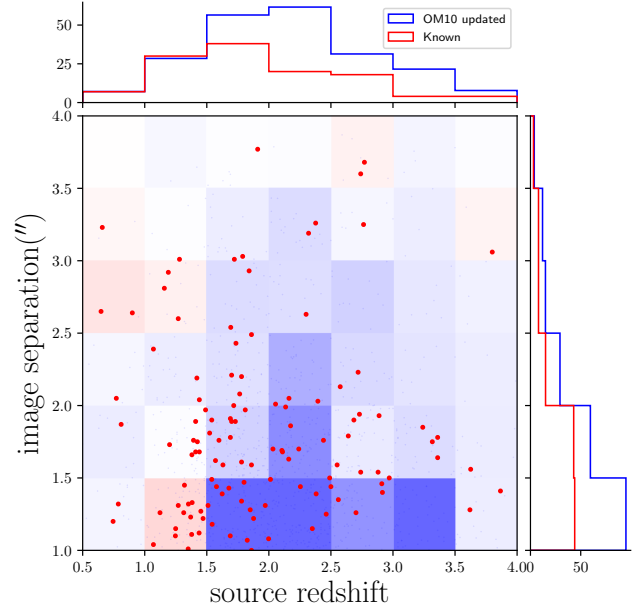


**Figure 19.** Distribution of image separations against source redshifts for a statistical sample of known lensed quasars (red) as described in the text. Circles are doubles, while squares are quads. Also overlaid in the histograms are the predicted numbers satisfying the same criteria from an updated version of the [Oguri & Marshall \(2010\)](#) mock catalogue; blue is an over-prediction relative to observed numbers, and red is an under-prediction.

the number of observed lenses by 44%, suggesting a discrepancy within their imposed galaxy velocity dispersion function, quasar luminosity function, or shear distribution.

## 5.2 Physical quasar pairs

We classify 11 systems as distinct quasar pairs at very similar redshifts. Following [Hennawi et al. \(2010\)](#), we take our operational definition of a binary quasar to have measured redshifts within  $2000 \text{ km s}^{-1}$ . This accounts for possible offsets of emission lines from the systemic redshift due to the dynamics of the broad line region, inflows/outflows, and absorption, while also allowing for peculiar velocities of the two quasars while still remaining in the same halo. The best-fit redshifts are found by minimising the  $\chi^2$  of fitting a quasar template using `PyQSOFIT` within a range of redshifts ([Guo et al. 2018](#)). Uncertainties are not quoted since they depend strongly on the prior for potential velocity offsets of certain lines. A summary of key parameters is given in Table 2. Of particular interest are the smallest-separation distinct quasar pairs, which probe the latest stage in the merger process and are the least well-characterised population. Only recently have binary quasars below sub-10kpc been discovered above redshift 1 ([Inada et al. 2008](#); [Anguita et al. 2018](#); [Tang et al. 2021](#)), due to typical ground-based observing conditions

**Table 2.** Summary of confirmed binary quasars. †The brighter component of J2355-4553 is a BAL quasar, and thus is compatible with two redshifts even when masking the absorption features. We quote the more likely lower redshift (2.832) and relevant velocity difference, but a redshift of 2.8506 ( $\Delta\theta = 60\text{kms}^{-1}$ ) is also possible.

Name	$z$	$\Delta v$ (kms $^{-1}$ )	$\Delta\theta$ (")	$d$ (kpc)
J0041-5350	0.5489, 0.5504	290	1.06	6.8
J0315-3522	0.4572, 0.4573	20	1.3	7.6
J0707+4109	0.5114, 0.5149	690	2.96	18.3
J0805+3550	1.6604, 1.6761	1760	1.13	9.6
J0939-0109	0.2240, 0.2247	170	1.9	6.8
J1116-2122	0.7094, 0.7106	210	3.29	23.6
J2121+1713	0.6298, 0.6307	170	2.89	19.8
J2132+3635	1.2135, 1.2148	180	1.33	11
J2256+2223	0.7506, 0.7534	480	1.63	12
J2322+0916	1.2064, 1.2066	30	4.51	37.4
J2355-4553†	2.8320, 2.8498	1390	2.20	17.2

and blending at such small angular separations (typically under 1 arcsecond). Lemon et al. (2022) argued that the discovery of the first lensed binary quasar (with a sub-10kpc source) likely suggests a larger population of unlensed small-separation binaries. Several convincing candidate systems are already being found using *Gaia* and *HST* follow-up imaging (Shen et al. 2021; Chen et al. 2022). We therefore expect to find such systems as a byproduct of a lensed quasar search. However, systems with residual flux between the putative lensed images are preferentially observed for spectroscopy, which explains our bias towards low-redshift distinct quasar pairs relative to the lensed quasar sources (median redshifts of 0.71 and 1.94 respectively).

### 5.3 Projected quasars

We report 11 new projected quasar pairs, with angular separations ranging from 0.98 - 4.64", and physical impact parameters from 6.2 - 34.3 kpc. We summarise the key parameters of these pairs in Table 3. Such systems are valuable for understanding quasar feedback by probing the host galaxy of the foreground quasar through absorption of the background quasar continuum (see the Quasars probing quasars paper series, e.g. Hennawi et al. 2006). Studies are typically limited to probing regions above 25 kpc from the foreground quasars (e.g. Johnson et al. 2015), since samples are built only from well-separated quasars (more likely to both have been targeted for spectroscopy). Of particular interest are the systems with small transverse proper distances (i.e. under 20 kpc) since they are both intrinsically rare ( $P(d) \sim d^2$ ), and are harder to discover due to observational constraints (e.g. systems become blended in ground-based imaging and are therefore not selected for spectroscopic follow-up as quasars). There are discrepancies between simulations and observations regarding Ly $\alpha$  absorption statistics below 100kpc in quasar host galaxies (Prochaska et al. 2013; Sorini et al. 2020), suggesting observational constraints on the absorption properties at small projected separations will be key to constraining more advanced feedback models.

The QSO pair Spectral Database of Findlay et al. (2018) lists only 4 projected quasar pairs with angular separations under 3 arcseconds and velocity differences above 2000 kms $^{-1}$  (after removing known lensed quasars and spurious cross-matches), compared to ~3000 such pairs with projections under 30 arcseconds. Sub-10-kpc-separation projected pairs from the literature have come from lens searches: DESJ0215-4728 ( $b=6.3$  kpc,  $z_{fg}=0.467$ , 1.07") from Anguita et al. (2018), J0240-0208 ( $b=7.6$  kpc,  $z_{fg}=1.058$ ,

**Table 3.** Summary of confirmed projected quasar pairs.

Name	$z_{fg}$	$z_{bg}$	$\Delta\theta$ (")	$d$ (kpc)
J0021+1927	1.045	1.09	2.89	23.4
J0027+0438	0.194	1.972	1.92	6.2
J0032-4523	1.667	1.74	2.34	19.8
J0249+2606	1.514	2.68	3.21	27.2
J0436+7851	0.765	1.975	4.64	34.3
J0553+0910	1.08	1.85	1.11	9.0
J0601-2220	0.809	0.836	0.98	7.4
J1820+3747	0.614	0.754	3.10	20.9
J2302-4154	0.98	1.22	1.22	9.7
J2314+0323	0.315	0.606	1.87	8.6
J2318+0250	1.83	1.945	3.23	27.2

0.94") from Shalyapin et al. (2018) and Anguita et al. (2018), and J2251+0016 ( $b=10.0$  kpc,  $z_{fg}=0.41$ , 1.86") from Tang et al. (2021). The projected quasars presented in this work almost triple the number of systems probing the foreground galaxies within 10 kpc (from 3 to 8 systems).

The number of such systems expected at each separation can be predicted through well-constrained quasar luminosity functions, along with the predicted luminosity and redshift distributions. We investigate this using the quasar luminosity function from Ross et al. (2013). We recover both the redshift distribution and absolute numbers of the spectroscopically confirmed quasar sample in a 500 square degree patch of SDSS. We estimate a sky density of quasars ( $0 < z < 4$ ) with *i*-band magnitude above 20.7 of  $\approx 30.0$  per square degree. In an area of 20,000 square degrees, this predicts 110 pairs within 5 arcseconds, and 17 pairs within 2 arcseconds. Several other studies report sub-2" projected pairs (Inada et al. 2008; More et al. 2016; Schechter et al. 2017). Including the previously mentioned systems, the total is  $\sim 10$ , below the predicted number which was a conservative value given some components of the known systems have  $i > 20.7$ . Designing searches to find these missing projected pairs should be considered in future lensed quasar and quasar pair searches.

Finally, we note that some of these systems could still be acting as strong lenses when the foreground galaxy is massive enough, and any counterimage is blended with the foreground host and is undetected in both the available low signal-to-noise imaging and spectra. High-resolution follow-up imaging would provide strong constraints on any such strong lensing, and, in the case of no detection, can still be used to obtain constraints on the mass profile (Smith et al. 2018).

### 5.4 Contaminants

It is prudent to reflect on the main contaminants from our search, principally to aid future discovery methods. Given the utility and rarity of small-separation projected and physical quasar pairs, we include them in our true positive sample. Of the 175 observed systems, 25 are confirmed as contaminant systems: 17 quasar+star/non-quasar, 5 star-forming galaxies, and 3 star pairs. Of the stellar pairs, two have red WISE colours similar to those of quasars, which are rare but a well-known contaminant in infrared-colour selection of quasars, and one (J1752+0826) was selected as a *Gaia* detection near a galaxy and whose Pan-STARRS image shows a very convincing possible lensed quasar. Of the 5 star-forming galaxies, one was a potential quad candidate selected through the single offset method, and the rest were *Gaia* multiplets around red WISE quasar candidates. Finally, of the 17 quasar+star pairs, 15 were selected as *Gaia* multiplets around WISE quasars, and 2 as *Gaia* singlets near

galaxies. We expect that future improvements in the *Gaia* catalogue – through more precise catalogue measurements – to continue to help remove such contaminants.

## 6 CONCLUSION

We have presented spectroscopic follow-up of 175 lensed quasar candidates, confirming 103 new lensed quasars, 17 of which simply lack photometric detection of the lensing galaxy, however, whose spectra are either very similar or whose imaging shows a faint counterimage. We also report 25 further unclassified quasar pairs which likely contain a mixture of lenses and distinct quasar pairs at the same redshift, however, further data is required in each case. We present 11 projected quasar pairs, and 11 binary pairs, which substantially increases the population of known systems at angular separations of a few arcseconds and below.

We used a mock catalogue of lensed quasars with an updated quasar luminosity function, galaxy velocity dispersion function, and treatment of shear to compare the current population of known lensed quasars with multiple *Gaia* detections. We show that the majority of lensed quasars with sources below redshift 1.5 are known, however, almost half of lenses with sources above  $z=1.5$  are yet to be discovered, which mostly have image separations below  $1.5''$ . The likely and possible lensed quasars discovered in this work represent already a subset of these missing lenses.

With the goal of creating a magnitude-limited sample of lensed quasars, future *Gaia* data releases should help through increasing completeness in detections at small separations, and reliable classification of quasars through increased precision of proper motions and parallaxes, as well as better variability constraints due to a longer baseline. To test for the completeness and biases of each lens search, other searches making use of spectroscopic and cadenced photometric datasets will be crucial. Such searches in LSST, making use of detecting nearby or extended variability, should not only be an efficient method for selecting lensed quasars but also for selecting small-separation physical quasar pairs and projected quasars (Kochanek et al. 2006; Chao et al. 2020). As targets become fainter and more numerous – with up to 400 lensed quasars with measured time delays in LSST (Liao et al. 2015) – a complete survey for spectroscopic redshifts must be carefully designed to convert these delays into a powerful probe of measuring the Hubble constant, with special consideration to minimising follow-up of common contaminants.

## ACKNOWLEDGEMENTS

We would like to thank Amanda S. Bosh and Stephen E. Levine for obtaining MagIC observations of lensed quasars.

This work is supported by the Swiss National Science Foundation (SNSF) and by the European Research Council (ERC) under the European Union’s Horizon 2020 research and innovation program (COSMICLENS: grant agreement No 787886). This work was supported by JSPS KAKENHI Grant Numbers JP22H01260, JP18K03693, JP20H05856, JP20H00181. T.A. acknowledges support from ANID-FONDECYT Regular 1190335, the Millennium Science Initiative ICN12\_009 and the ANID BASAL project FB210003. TT acknowledges support by the National Science Foundation through grant NSF-AST-1906976. Support for this work was provided by NASA through the NASA Hubble Fellowship grant HST-HF2-51492 awarded to AJS by the Space Telescope Science

Institute, which is operated by the Association of Universities for Research in Astronomy, Inc., for NASA, under contract NAS5-26555.

This paper includes data gathered with the 6.5 meter Magellan Telescopes located at Las Campanas Observatory, Chile. This research used the facilities of the Canadian Astronomy Data Centre operated by the National Research Council of Canada with the support of the Canadian Space Agency.

This research has made use of the VizieR catalogue access tool, CDS, Strasbourg, France (DOI: 10.26093/cds/vizieR). The original description of the VizieR service was published in A&AS 143, 23.

This research has made use of the NASA/IPAC Extragalactic Database (NED), which is funded by the National Aeronautics and Space Administration and operated by the California Institute of Technology.

The Pan-STARRS1 Surveys (PS1) and the PS1 public science archive have been made possible through contributions by the Institute for Astronomy, the University of Hawaii, the Pan-STARRS Project Office, the Max-Planck Society and its participating institutes, the Max Planck Institute for Astronomy, Heidelberg and the Max Planck Institute for Extraterrestrial Physics, Garching, The Johns Hopkins University, Durham University, the University of Edinburgh, the Queen’s University Belfast, the Harvard-Smithsonian Center for Astrophysics, the Las Cumbres Observatory Global Telescope Network Incorporated, the National Central University of Taiwan, the Space Telescope Science Institute, the National Aeronautics and Space Administration under Grant No. NNX08AR22G issued through the Planetary Science Division of the NASA Science Mission Directorate, the National Science Foundation Grant No. AST-1238877, the University of Maryland, Eotvos Lorand University (ELTE), the Los Alamos National Laboratory, and the Gordon and Betty Moore Foundation.

The Legacy Surveys consist of three individual and complementary projects: the Dark Energy Camera Legacy Survey (DECaLS; Proposal ID #2014B-0404; PIs: David Schlegel and Arjun Dey), the Beijing-Arizona Sky Survey (BASS; NOAO Prop. ID #2015A-0801; PIs: Zhou Xu and Xiaohui Fan), and the Mayall z-band Legacy Survey (MzLS; Prop. ID #2016A-0453; PI: Arjun Dey). DECaLS, BASS and MzLS together include data obtained, respectively, at the Blanco telescope, Cerro Tololo Inter-American Observatory, NSF’s NOIRLab; the Bok telescope, Steward Observatory, University of Arizona; and the Mayall telescope, Kitt Peak National Observatory, NOIRLab. The Legacy Surveys project is honored to be permitted to conduct astronomical research on Iolkam Du’ag (Kitt Peak), a mountain with particular significance to the Tohono O’odham Nation.

NOIRLab is operated by the Association of Universities for Research in Astronomy (AURA) under a cooperative agreement with the National Science Foundation.

This project used data obtained with the Dark Energy Camera (DECam), which was constructed by the Dark Energy Survey (DES) collaboration. Funding for the DES Projects has been provided by the U.S. Department of Energy, the U.S. National Science Foundation, the Ministry of Science and Education of Spain, the Science and Technology Facilities Council of the United Kingdom, the Higher Education Funding Council for England, the National Center for Supercomputing Applications at the University of Illinois at Urbana-Champaign, the Kavli Institute of Cosmological Physics at the University of Chicago, Center for Cosmology and Astro-Particle Physics at the Ohio State University, the Mitchell Institute for Fundamental Physics and Astronomy at Texas A&M University, Financiadora de Estudos e Projetos, Fundacao Carlos Chagas Filho de Amparo, Financiadora de Estudos e Projetos, Fundacao

Carlos Chagas Filho de Amparo a Pesquisa do Estado do Rio de Janeiro, Conselho Nacional de Desenvolvimento Científico e Tecnológico and the Ministerio da Ciencia, Tecnologia e Inovacao, the Deutsche Forschungsgemeinschaft and the Collaborating Institutions in the Dark Energy Survey. The Collaborating Institutions are Argonne National Laboratory, the University of California at Santa Cruz, the University of Cambridge, Centro de Investigaciones Energeticas, Medioambientales y Tecnologicas-Madrid, the University of Chicago, University College London, the DES-Brazil Consortium, the University of Edinburgh, the Eidgenossische Technische Hochschule (ETH) Zurich, Fermi National Accelerator Laboratory, the University of Illinois at Urbana-Champaign, the Institut de Ciències de l'Espai (IEEC/CSIC), the Institut de Física d'Altes Energies, Lawrence Berkeley National Laboratory, the Ludwig Maximilians Universität München and the associated Excellence Cluster Universe, the University of Michigan, NSF's NOIRLab, the University of Nottingham, the Ohio State University, the University of Pennsylvania, the University of Portsmouth, SLAC National Accelerator Laboratory, Stanford University, the University of Sussex, and Texas A&M University.

BASS is a key project of the Telescope Access Program (TAP), which has been funded by the National Astronomical Observatories of China, the Chinese Academy of Sciences (the Strategic Priority Research Program “The Emergence of Cosmological Structures” Grant # XDB09000000), and the Special Fund for Astronomy from the Ministry of Finance. The BASS is also supported by the External Cooperation Program of Chinese Academy of Sciences (Grant # 114A11KYSB20160057), and Chinese National Natural Science Foundation (Grant # 11433005).

The Legacy Survey team makes use of data products from the Near-Earth Object Wide-field Infrared Survey Explorer (NEOWISE), which is a project of the Jet Propulsion Laboratory/California Institute of Technology. NEOWISE is funded by the National Aeronautics and Space Administration.

The Legacy Surveys imaging of the DESI footprint is supported by the Director, Office of Science, Office of High Energy Physics of the U.S. Department of Energy under Contract No. DE-AC02-05CH1123, by the National Energy Research Scientific Computing Center, a DOE Office of Science User Facility under the same contract; and by the U.S. National Science Foundation, Division of Astronomical Sciences under Contract No. AST-0950945 to NOAO.

## REFERENCES

- Anguita T., et al., 2018, *MNRAS*, **480**, 5017
- Bernardi M., Shankar F., Hyde J. B., Mei S., Marulli F., Sheth R. K., 2010, *MNRAS*, **404**, 2087
- Blanton M. R., et al., 2017, *AJ*, **154**, 28
- Chae K.-H., 2003, *MNRAS*, **346**, 746
- Chambers K. C., et al., 2016, arXiv e-prints, p. arXiv:1612.05560
- Chan J. H. H., et al., 2022, *A&A*, **659**, A140
- Chao D. C. Y., Chan J. H. H., Suyu S. H., Yasuda N., More A., Oguri M., Morokuma T., Jaelani A. T., 2020, *A&A*, **640**, A88
- Chen Y.-C., Hwang H.-C., Shen Y., Liu X., Zakamska N. L., Yang Q., Li J. I., 2022, *ApJ*, **925**, 162
- Citro A., Erb D. K., Pettini M., Auger M. W., Becker G. D., James B. L., 2021, *ApJ*, **922**, 187
- Collett T. E., Auger M. W., 2014, *MNRAS*, **443**, 969
- Croom S. M., Smith R. J., Boyle B. J., Shanks T., Miller L., Outram P. J., Loaring N. S., 2004, *MNRAS*, **349**, 1397
- Delchambre L., et al., 2019, *A&A*, **622**, A165
- Desira C., Shu Y., Auger M. W., McMahon R. G., Lemon C. A., Anguita T., Neira F., 2022, *MNRAS*, **509**, 738
- Dey A., et al., 2019, *AJ*, **157**, 168
- Fan X., et al., 2019, *ApJ*, **870**, L11
- Findlay J. R., et al., 2018, *ApJS*, **236**, 44
- Flesch E. W., 2015, *Publ. Astron. Soc. Australia*, **32**, e010
- Foreman-Mackey D., Hogg D. W., Lang D., Goodman J., 2013, *PASP*, **125**, 306
- Gaia Collaboration et al., 2018, *A&A*, **616**, A1
- Gordon Y. A., et al., 2021, VizieR Online Data Catalog, p. J/ApJS/255/30
- Guo H., Shen Y., Wang S., 2018, PyQSOFit: Python code to fit the spectrum of quasars, Astrophysics Source Code Library (ascl:1809.008)
- Harvey D., 2020, *MNRAS*, **498**, 2871
- Hennawi J. F., et al., 2006, *ApJ*, **651**, 61
- Hennawi J. F., et al., 2010, *ApJ*, **719**, 1672
- Holden B. P., Nichol R. C., Romer A. K., Metevier A., Postman M., Ulmer M. P., Lubin L. M., 1999, *AJ*, **118**, 2002
- Huchra J., Gorenstein M., Kent S., Shapiro I., Smith G., Horine E., Perley R., 1985, *AJ*, **90**, 691
- Hurley-Walker N., et al., 2017, *MNRAS*, **464**, 1146
- Hutsemékers D., Sluse D., 2021, *A&A*, **654**, A155
- Hutsemékers D., Borguet B., Sluse D., Riaud P., Anguita T., 2010, *A&A*, **519**, A103
- Inada N., et al., 2008, *AJ*, **135**, 496
- Jaelani A. T., et al., 2021, *MNRAS*, **502**, 1487
- Jiménez-Vicente J., Mediavilla E., 2019, *ApJ*, **885**, 75
- Johnson S. D., Chen H.-W., Mulchaey J. S., 2015, *MNRAS*, **452**, 2553
- Kassiola A., Kovner I., Blandford R. D., 1992, *ApJ*, **396**, 10
- Kayo I., et al., 2007, *AJ*, **134**, 1515
- Kochanek C. S., Mochejska B., Morgan N. D., Stanek K. Z., 2006, *ApJ*, **637**, L73
- Korista K. T., Voit G. M., Morris S. L., Weymann R. J., 1993, *ApJS*, **88**, 357
- Krone-Martins A., et al., 2019, arXiv e-prints, p. arXiv:1912.08977
- Lang D., Hogg D. W., Schlegel D. J., 2016, *AJ*, **151**, 36
- Lemon C. A., Auger M. W., McMahon R. G., Kposov S. E., 2017, *MNRAS*, **472**, 5023
- Lemon C. A., Auger M. W., McMahon R. G., Ostrovski F., 2018, *MNRAS*, **479**, 5060
- Lemon C. A., Auger M. W., McMahon R. G., 2019, *MNRAS*, **483**, 4242
- Lemon C., Millon M., Sluse D., Courbin F., Auger M., Chan J. H. H., Paic E., Agnello A., 2022, *A&A*, **657**, A113
- Liao K., et al., 2015, *ApJ*, **800**, 11
- Lucey J. R., Schechter P. L., Smith R. J., Anguita T., 2018, *MNRAS*, **476**, 927
- Mainzer A., et al., 2011, *ApJ*, **743**, 156
- Mauch T., Murphy T., Buttery H. J., Curran J., Hunstead R. W., Piestrzynski B., Robertson J. G., Sadler E. M., 2003, *MNRAS*, **342**, 1117
- McKean J. P., et al., 2005, *MNRAS*, **356**, 1009
- Mediavilla E., Jiménez-Vicente J., Muñoz J. A., Vives-Arias H., Calderón-Infante J., 2017, *ApJ*, **836**, L18
- Moffat A. F. J., 1969, *A&A*, **3**, 455
- More A., et al., 2016, *MNRAS*, **456**, 1595
- Muchovej S., et al., 2010, *ApJ*, **716**, 521
- Myers S. T., et al., 2003, *MNRAS*, **341**, 1
- Ochsenbein F., Bauer P., Marcout J., 2000, *A&AS*, **143**, 23
- Oguri M., 2018, *MNRAS*, **480**, 3842
- Oguri M., Marshall P. J., 2010, *MNRAS*, **405**, 2579
- Oguri M., et al., 2006, *AJ*, **132**, 999
- Oguri M., et al., 2012, *AJ*, **143**, 120
- Okoshi K., et al., 2021, *AJ*, **162**, 175
- Orban de Xivry G., Marshall P., 2009, *MNRAS*, **399**, 2
- Ostrovski F., et al., 2018, *MNRAS*, **473**, L116
- Paic E., Vernardos G., Sluse D., Millon M., Courbin F., Chan J. H., Bonvin V., 2022, *A&A*, **659**, A21
- Planck Collaboration et al., 2020, *A&A*, **641**, A6
- Prochaska J. X., et al., 2013, *ApJ*, **776**, 136
- Rankine A. L., Hewett P. C., Banerji M., Richards G. T., 2020, *MNRAS*, **492**, 4553
- Reimers D., Hagen H. J., Baade R., Lopez S., Tytler D., 2002, *A&A*, **382**, L26

- Riello M., et al., 2021, *A&A*, 649, A3
- Ross N. P., et al., 2013, *ApJ*, 773, 14
- Rubin K. H. R., et al., 2018, *ApJ*, 859, 146
- Rusu C. E., Oguri M., Minowa Y., Iye M., More A., Inada N., Oya S., 2014, *MNRAS*, 444, 2561
- Saxton R. D., Read A. M., Esquej P., Freyberg M. J., Altieri B., Bermejo D., 2008, *A&A*, 480, 611
- Schechter P. L., Wambsganss J., 2002, *ApJ*, 580, 685
- Schechter P. L., Pooley D., Blackburne J. A., Wambsganss J., 2014, *ApJ*, 793, 96
- Schechter P. L., Morgan N. D., Chehade B., Metcalfe N., Shanks T., McDonald M., 2017, *AJ*, 153, 219
- Schindler J.-T., et al., 2018, *ApJ*, 863, 144
- Schmidt T., et al., 2022, arXiv e-prints, p. [arXiv:2206.04696](https://arxiv.org/abs/2206.04696)
- Sérsic J. L., 1963, Boletín de la Asociación Argentina de Astronomía La Plata Argentina, 6, 41
- Shajib A. J., et al., 2020, *MNRAS*, 494, 6072
- Shalyapin V. N., Sergeev A. V., Goicoechea L. J., Zheleznyak A. P., 2018, *MNRAS*, 480, 2853
- Shen Y., et al., 2021, *Nature Astronomy*, 5, 569
- Shin E. M., Evans N. W., 2008, *MNRAS*, 390, 505
- Sluse D., Hutsemékers D., Anguita T., Braibant L., Riaud P., 2015, *A&A*, 582, A109
- Smith R. J., Lucey J. R., Collier W. P., 2018, *MNRAS*, 481, 2115
- Sonnenfeld A., et al., 2020, *A&A*, 642, A148
- Sorini D., Davé R., Anglés-Alcázar D., 2020, *MNRAS*, 499, 2760
- Spiniello C., et al., 2018, *MNRAS*, 480, 1163
- Spiniello C., Agnello A., Sergeev A. V., Anguita T., Rodríguez Ó., Napolitano N. R., Tortora C., 2019, *MNRAS*, 483, 3888
- Stern D., et al., 2012, *ApJ*, 753, 30
- Stern D., et al., 2021, *ApJ*, 921, 42
- Tang S., et al., 2021, *ApJ*, 922, 83
- Torrey P., et al., 2015, *MNRAS*, 454, 2770
- Treu T., et al., 2018, *MNRAS*, 481, 1041
- Wang S., Liu J., Qiu Y., Bai Y., Yang H., Guo J., Zhang P., 2016, *ApJS*, 224, 40
- Webb N. A., et al., 2020, *A&A*, 641, A136
- Yue M., Fan X., Yang J., Wang F., 2022, arXiv e-prints, p. [arXiv:2201.06761](https://arxiv.org/abs/2201.06761)
- Zhou R., et al., 2021, *MNRAS*, 501, 3309

This paper has been typeset from a  $\text{\TeX}/\text{\LaTeX}$  file prepared by the author.